Astron Astrophys Rev (2008) 16:155–208
DOI 10.1007/s00159-008-0014-9

REVIEW ARTICLE

Hard X-ray emission from the solar corona

S. Krucker · M. Battaglia · P. J. Cargill · L. Fletcher · H. S. Hudson · A. L. MacKinnon · S. Masuda · L. Sui · M. Tomczak · A. L. Veronig · L. Vlahos · S. M. White

Received: 4 December 2007 / Published online: 1 October 2008

Abstract This review surveys hard X-ray emissions of non-thermal electrons in the solar corona. These electrons originate in flares and flare-related processes. Hard X-ray emission is the most direct diagnostic of electron presence in the corona, and such observations provide quantitative determinations of the total energy in the non-thermal electrons. The most intense flare emissions are generally observed from the

S. Krucker (✉) · H. S. Hudson
Space Sciences Laboratory, University of California,
Berkeley, CA 94720-7450, USA
e-mail: krucker@ssl.berkeley.edu

M. Battaglia
Institute of Astronomy, ETH Zurich, 8093 Zurich, Switzerland

P. J. Cargill
Space and Atmospheric Physics, Blackett Laboratory, Imperial College,
London SW7 2BW, UK

L. Fletcher
Department of Physics and Astronomy, University of Glasgow,
Glasgow G12 8QQ, UK

A. L. MacKinnon
DACE/Department of Physics and Astronomy, University of Glasgow,
Glasgow G12 8QQ, UK

S. Masuda
Solar-Terrestrial Environment Laboratory, Nagoya University,
Furo-cho, Chikusa-ku, Nagoya, 4648601, Japan

L. Sui
NASA Goddard Space Flight Center, Solar Physics Laboratory,
Code 671, Greenbelt, MD 20771, USA

chromosphere at footpoints of magnetic loops. Over the years, however, many observations of hard X-ray and even γ-ray emission directly from the corona have also been reported. These coronal sources are of particular interest as they occur closest to where the electron acceleration is thought to occur. Prior to the actual direct imaging observations, disk occultation was usually required to study coronal sources, resulting in limited physical information. Now RHESSI[1] has given us a systematic view of coronal sources that combines high spatial and spectral resolution with broad energy coverage and high sensitivity. Despite the low density and hence low bremsstrahlung efficiency of the corona, we now detect coronal hard X-ray emissions from sources in all phases of solar flares. Because the physical conditions in such sources may differ substantially from those of the usual "footpoint" emission regions, we take the opportunity to revisit the physics of hard X-radiation and relevant theories of particle acceleration.

Keywords Sun · Corona · Hard X-rays

Contents

[1] The Reuven Ramaty High-Energy Solar Spectroscopic Imager; see Lin et al. (2002).

M. Tomczak
Astronomical Institute, University of Wroclaw,
ul. Kopernika 11, 51-622 Wroclaw, Poland

A. L. Veronig
Institute of Physics/IGAM, University of Graz,
Universitätsplatz 5, 8010 Graz, Austria

L. Vlahos
Department of Physics, University of Thessaloniki,
Thessaloniki, 54124, Greece

S. M. White
Astronomy Department, University of Maryland,
College Park, MD 20742, USA

1 Introduction

The study of hard X-ray emission from solar flares is a relatively mature field. Our systematic knowledge, however, relates mainly to the radiation produced near the solar surface when energetic electrons interact with nuclei in the dense solar chromosphere at the footpoints of coronal magnetic loops. Hard X-ray emission from the corona itself, the subject of this review, is much less well understood, and presents some dramatically different properties.

The hard X-rays of the impulsive phase are generally described as "thick target footpoint emission:" "thick target," because the chromosphere is dense enough to stop the electrons completely by Coulomb and ionizing collisions; and "footpoint," because it arises at the base of the coronal magnetic loops that guide the motion of the electrons. The theory of thick-target bremsstrahlung is well-understood quantitatively. The high density of the chromosphere is crucial in this picture, since the production of ordinary thin-target bremsstrahlung photons is proportional to the density of the target. Within this framework, little significant hard X-ray emission is expected from the corona itself because the density there is so much lower. In the usual thick-target model, the electrons propagate essentially unimpeded through the coronal portions

of the magnetic loops, following their acceleration in a yet-to-be-identified coronal source.

In most flares the hard X-ray emission is indeed dominated by footpoint sources, but it is increasingly evident that there are coronal hard X-ray sources that do not fit this picture very well. The meter-wave radio sources (see e.g. Wild et al. 1963) anticipated this by revealing the presence of diverse coronal populations of energetic electrons. An early example of coronal hard X-ray emission was the detection by OSO-5 of X-rays up to 220 keV from a flare estimated to have been 20° behind the limb, so that the minimum height of the X-ray emission above the photosphere was 40,000 km (Frost and Dennis 1971; Palmer and Smerd 1972). The geometry for this event thus precluded any contribution from the dense atmospheric layers below the transition region. The low plasma density at such a coronal height would normally imply low hard X-ray emissivity, resulting in fluxes below detection thresholds in most events. More recently, RHESSI observed 100 keV hard X-rays above the limb from a flare at least 40° behind the limb, so that the height of the source may have been over 150,000 km (some 0.2 $R_{\odot}$). The hard X-rays were seen at this height at the onset of the event, i.e., with no appreciable delay relative to emission at lower heights in the corona (Krucker et al. 2007b).

This paper summarizes the recent observational material on hard X-ray emission from sources in the solar corona, and discusses how these results influence our understanding of particle acceleration, propagation and trapping in solar flares. This is a timely exercise thanks to the results from the RHESSI satellite (Lin et al. 2002), which has provided excellent imaging at photon energies from 3 keV to 10 MeV since 2002 (see Cliver et al. 1986, for a review of the earliest observations). In this paper we also discuss the pioneering hard X-ray imaging observations from the *Yohkoh* satellite (Kosugi et al. 1992). Coronal hard X-ray sources continue to pose difficult observational problems, because current imaging techniques at such high photon energies have limited imaging dynamic range. When intense footpoint sources are present, they can soak up the available image dynamic range and prevent detection of weaker coronal sources. Events from over the limb in which the footpoint sources are occulted continue to be a valuable resource for the study of coronal emission, but there are also many events in which the coronal sources can now be detected for events on the solar disk, and the variety of properties they exhibit is a challenge to existing ideas.

We describe these properties using specific examples, and discuss their implications for flare physics. In particular, one of the best known of all coronal hard X-ray sources was found in the famous "Masuda flare" (Masuda et al. 1994), Sect. 2.2.2, which has been the focus of an extraordinary amount of discussion over the last decade and has strongly motivated the standard magnetic-reconnection model of solar flares. This model envisions a magnetic eruption followed by the sequential reconnection of field lines at greater and greater heights, resulting in the various flare effects. In this paper we will frequently appeal to this conceptual framework, even though it may not relate well to some of the coronal hard X-ray observations. Readers unfamiliar with this scheme should refer to Sect. 3.3.1 for an overview.

In the following (Sect. 2) we describe observations of coronal hard X-ray sources organized by their occurrence in the pre-flare, impulsive and late phases of flares; please

see Sect. 2.5 and Table 1 for a shortcut summary. The Table lists ten morphologies of coronal hard X-ray emission, all distinct from the classical footpoint sources. We note that we are possibly seeing non-standard paradigms for hard X-ray production in the coronal hard X-ray sources, and to the extent that new physics is indeed required, stellar or other non-solar astrophysicists may benefit from the new analogs these observations offer. The basic physics of the production of hard X-rays is revisited in Appendix A, and the coronal time scales for particles in Appendix B. Understanding how hard X-rays can be produced in the low-density environment of the solar corona poses interesting problems, and we discuss theoretical ideas in Sect. 3 (see Miller et al. 1997, for a comparable earlier overview).

2 Observations

We arrange the observational material in chronological sequence of flare development, generally illustrating the phenomena with specific flare events. We wish to emphasize at the outset that we are looking for new paradigms that differ from the standard impulsive-phase pattern characterized by bright hard X-ray footpoints (Hoyng et al. 1981; Hudson and Ryan 1995), the Neupert effect (Neupert 1968; Dennis and Zarro 1993; Veronig et al. 2005b), and the soft-hard-soft spectral pattern[2] (Parks and Winckler 1969; Hudson and Fárník 2002; Grigis and Benz 2004). At the end we also review some statistical studies in Sect. 2.4, and then summarize everything in Table 1.

2.1 Early phase

The RHESSI observations have given us what appears to be a new class of coronal hard X-ray sources, namely coronal sources that *precede* the impulsive phase. The prototype of this class is the event of 23 July 2002 (Lin et al. 2003; Asai et al. 2006), and the events of 3 November 2003 10 UTC (Veronig et al. 2006) and 24 August 2002 may also belong to this category. The 23 July 2002 event occurred just inside the east limb and exhibited a pair of ribbons in the chromosphere in TRACE[3] 195 Å images. The first > 10 keV hard X-ray source seen in this event by RHESSI occurs in the corona, located clearly above and between the chromospheric ribbons (Fig. 1), at a time when no hard X-ray footpoint sources are visible. Lin et al. (2003) pointed out that the hard X-ray spectrum in this phase of the event appears almost continuous to low energies ($<$10 keV), but with the characteristic Fe emission feature at 6.7 keV establishing that some background thermal plasma with flare-like temperatures[4] (above about 8 MK; Phillips 2004) exists in the source. While the time evolution of the thermal component is gradual, the emission at higher energies shows time variations at 10–30 s duration,

[2] In the soft-hard-soft (SHS) spectral pattern, hardness correlates with flux; in the soft-hard-harder pattern (SHH) the spectrum progressively hardens.

[3] Transition region and coronal explorer (Handy et al. 1999).

[4] "Temperature" in this paper means the electron temperature T_e unless otherwise stated.

Table 1 Coronal hard X-ray sources: representative parameters

Type[a]	Phase[b]	Archetype (date/month/year)	Number studied	Height (Mm)	E_{obs} (keV)	F_{30}[c]	γ[d]	Density[e] (cm^{-3})	Δt (min)	Scale (Mm)	Velocity[f] ($km\ s^{-1}$)
Early (Lin et al. 2003)	(1)	23/07/2002	3	20	<100	10	5	$\approx 10^{10}$	5	5	Small
Masuda (Masuda et al. 1994)	(2)	13/01/1992	<10	20	25–50	0.2	3–4.5	$<10^{9}$	2	5	Small
Coronal thick (Veronig and Brown 2004)	(2)	14/04/2002	≈5	20	<50	1	6–7	$\approx 10^{11}$	5–15	10	Small
Fast ejecta (Hudson et al. 2001)	(2)	18/04/2001	2	>100	<100	0.1	4	$\approx 4\times 10^{9}$	5	>20	$\approx 10^{3}$
High coronal (Kane et al. 1992)	(2–3)	16/02/1984	10	>100	<100	0.1	3–5	$<10^{9}$	5	>100	$\approx 10^{3}$
Superhot (Lin et al. 1981)	(2–3)	27/06/1980	Many	20	<40	100	Th	–	5–30	–	–
Double (Sui and Holman 2003)	(2)	15/04/2002	3	30	15–25	–	Th	$\approx 10^{10}$	≈3	10	Complex
Occulted (Zirin et al. 1969)	(2–3)	02/12/1967	Many	20	10–50	0.5	4–7	$\approx 10^{10}$	1–30	10	Small
Late phase (Frost and Dennis 1971)	(3)	30/03/1969	10	40	30–250	2	2	–	10–100	–	–
MeV (Krucker et al. 2008)	(2–3)	20/01/2005	3	20	200–10^{3}	2[g]	2	$\approx 10^{10}$	10	<20	–
Footpoints (Hoyng et al. 1981)	(1–3)	21/05/1980	Many	–	5–10^{3}	100	2–5	$>10^{12}$	0.1–30	<3	–

[a] Not intended as a classification scheme
[b] Event phase: (1) pre-impulsive; (2) impulsive; (3) late
[c] Peak flux reported, in [photons $(cm^2\ s\ keV)^{-1}$] at 30 keV
[d] Th = Thermal
[e] Electron density (n_e) in source
[f] Apparent radial velocity
[g] Extrapolation

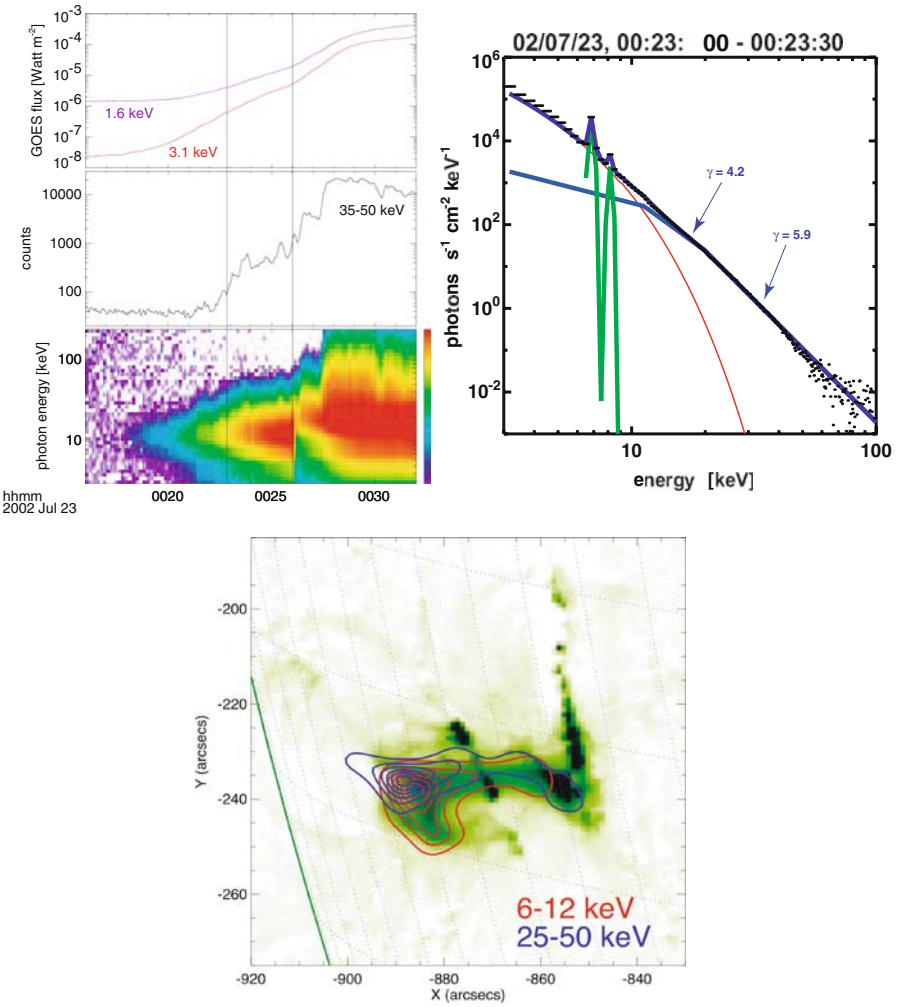

Fig. 1 Example of coronal emission before the impulsive phase in the 23 July 2002 flare. *Top left* X-ray time profiles and spectrogram from GOES and RHESSI, showing thermal emission with a gradual evolution and a second component at higher energy with fast time variations of tens of seconds. *Top right* photon spectrum with thermal fit (*red*) including fits to the Fe and Fe/Ni complexes (Phillips 2004), and non-thermal fit in *blue*. *Bottom* imaging reveals that the fast time variation component mostly comes from the corona. RHESSI contours in the thermal range (*red*) and at higher energies (*blue*) are shown for the time range outlined by *vertical bars* in the panel to the *left*. The image shown is a TRACE 195Å image taken at 00:26:00 UTC

suggesting that the two components come from different emission plasma components. X-ray spectral fitting reveals a relatively flat spectrum that can either be represented by a (broken) power law[5] (with photon power law index $\gamma \approx 5$), or by a multi-thermal fit

[5] In this paper we normally describe the spectral photon flux by a power law $(h\nu)^{-\gamma}$, and the electron number spectrum by $E^{-\delta}$, both indices positive.

with temperatures up to 100 MK. However, microwave observations (Asai et al. 2006) indicate the presence of non-thermal electrons at this time. Comparing hard X-ray and microwave observations of the 23 July 2002 event, Asai et al. (2006) found that a single population of non-thermal electrons could produce both emissions, although rather strong coronal magnetic field strengths (around 200 G) are needed to match the intensities seen in hard X-rays and microwaves.

The weakness of the footpoint emission in this phase distinguishes it from the thick-target model; normally with a hot thermal plasma trapped in coronal loops of low pre-flare density, one would expect that the non-thermal electrons would precipitate and produce strong footpoint emission.

2.2 Impulsive phase

2.2.1 Footpoint emission

Most of the impulsive-phase hard X-ray emission comes from the footpoint regions, as described by the thick-target model and originally observed with hard X-ray imaging observations from the Solar Maximum Mission (Hoyng et al. 1981). The morphology of these sources, in summary, includes the SHS spectral evolution pattern (Parks and Winckler 1969; Hudson and Fárník 2002), "chromospheric evaporation" (e.g., Antiochos and Sturrock 1978), the Neupert effect (Neupert 1968; Veronig et al. 2005b), type III radio bursts at longer wavelengths, and gyrosynchrotron emission at shorter wavelengths, etc.; the newer observations show these as well as the other patterns of behavior described in this paper.

2.2.2 The "Masuda flare"

The *Yohkoh* observations of what is now universally termed the "Masuda flare" (Masuda et al. 1994) showed the presence of high-energy electrons in the corona during the impulsive phase of a limb event (see Fig. 2). Besides the classic flare pic-

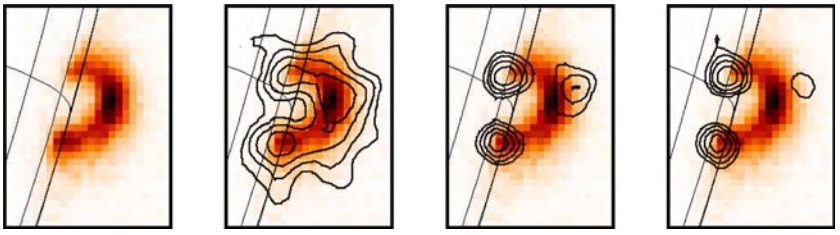

Fig. 2 Hard X-ray and soft X-ray images of the 13 January 1992 flare. The *leftmost panel* shows a soft X-ray image taken with the *Yohkoh*/SXT Be filter at 17:28:07 UTC. From *left* to *right*, the remaining three panels show image contours at 14–23, 23–33, and 33–53 keV, respectively, taken from 17:27:35 to 17:28:15 UTC by *Yohkoh*/HXT, overlaid on the same soft X-ray image. The contour levels are 6.25, 12.5, 25.0 and 50.0% of the peak value. The field of view is $59'' \times 79''$ for all panels. The hard X-ray contours shown were derived using a later calibration and are therefore slightly different from the original publication (Masuda et al. 1994)

ture with a thermal loop and two hard X-ray footpoints, the Masuda flare reveals a coronal hard X-ray source located ≈7,000 km above the thermal loop (see Fig. 2). The coronal emission is best seen between between 30 and 50 keV, is rather compact (3,500–7,000 km), and has a time evolution similar (within the time resolution of tens of seconds) to that of the footpoints. The emission occurs in the impulsive phase and consists of a single peak that lasts for about 2 min. Surprisingly, no enhanced soft X-ray emission was detected at the location of the coronal hard X-ray source, indicating a rather low thermal plasma density (Hudson and Ryan 1995), although the electron temperature might have been rather high. The apparent temperature of the loops below the coronal hard X-ray source increased with height, suggesting an even higher (>30 MK) temperature at the location of the hard X-ray source. Such an effect is often evident in soft X-ray images of flare loop systems, such as the extreme example the Masuda flare itself presents. After the impulsive phase, all coronal emission became thermal at rather high temperatures, up to 40 MK (Nitta et al. 2001).

Yohkoh provided only four hard X-ray energy bands, covering the range 14–93 keV (Kosugi et al. 1991), and hence gave limited spectral information. Spectral shapes are derived by calculating flux ratios between pairs of energy channels. For the footpoints, all three ratios gave similar results at impulsive-phase maximum, and the spectrum could be represented by a single power-law spectrum with γ_{fp} of about 4 (Alexander and Metcalf 1997). However, the coronal hard X-ray source was surprisingly weak in the 14–23 keV channel, if present at all, having a flatter/harder spectrum below ≈20 keV than above. This makes a thermal explanation problematic, as the temperature derived from the lower channels is higher (T > 300 MK) than the temperature from the higher channels ($T = 120 \pm 15$ MK). Alexander and Metcalf (1997) therefore concluded that the coronal hard X-ray emission had a non-thermal origin, with a power-law slope of $\gamma_1 = 2.2 \pm 0.6$ below ≈25 keV and $\gamma_2 = 4.1 \pm 0.2$ above. Their comparison of the footpoint and coronal spectra showed the coronal spectrum to be inconsistent with thin-target emission from the same electrons that later produce the footpoint sources as thick-target emission. The flatness of the low-energy spectrum also suggests an interpretation in terms of a low-energy cutoff in the electron distribution.

Although several somewhat similar events have been published (Masuda 1994; Tomczak 2001; Petrosian et al. 2002), the Masuda event has not proven to be typical of solar flares in general. The similar events show less separation (<3,500 km) between the thermal soft X-ray loops and the coronal hard X-ray source (e.g., Krucker et al. 2007a), and many filled-loop events even show co-spatial non-thermal emission (Tomczak 2001; Krucker and Lin 2008).

The novel features of the coronal source of the original Masuda flare were its location *above* the soft X-ray looptop during the impulsive phase, and a non-thermal spectral signature. The paper originally describing the Masuda flare (Masuda et al. 1994) has been cited many hundreds of times, and has had an enormous influence on the development of flare theory. The morphology matched the cusp geometry commonly taken to imply the presence of a magnetic X-point above the flaring loops. The evident presence of non-thermal particles in this geometry then led to much discussion of the classical large-scale magnetic reconnection models of solar flares, as originally cited by Masuda et al. themselves (see the further discussion in Sect. 3.3.1).

2.2.3 Double coronal sources

Sui and Holman (2003) and Sui et al. (2004) studied a series of homologous limb flares that occurred during 14–16 April 2002, in which a coronal thermal X-ray source, detectable up to about 20 keV photon energy and above the flare loops, was observed early in the impulsive phase. Note that some of these unusual flares also have a "coronal thick target" interpretation at higher energies, as discussed below in Sect. 2.2.4. The coronal source was stationary for several minutes and eventually moved outward at a speed of ≈300 km s^{-1} (Sui and Holman 2003). Spectrally resolved X-ray imaging of flare loops typically shows that the hotter X-ray sources are located *above* the not-so-hot ones, whereas for these coronal sources we see the exact opposite (Fig. 3). The normal temperature pattern is interpreted in the standard model (Sect. 3.3.1) in a natural way by the time sequence of reconnection. The inverted temperature gradient in the coronal sources now detected above the loop-top sources is entirely novel and unexpected. The morphology suggests that the highest temperatures lie between the loop and coronal X-ray sources, but that the emission measure there (small volume and/or low density) is too low to provide detectable emission. Sui et al. (2004) interpreted this finding as evidence for a current sheet formed between the tops of the flare loops and the coronal sources above the loops. An occulted event of 30 April 2002 showed similar coronal structure (Liu et al. 2008), again with the above-the-loop coronal source showing an inverted temperature/energy gradient.

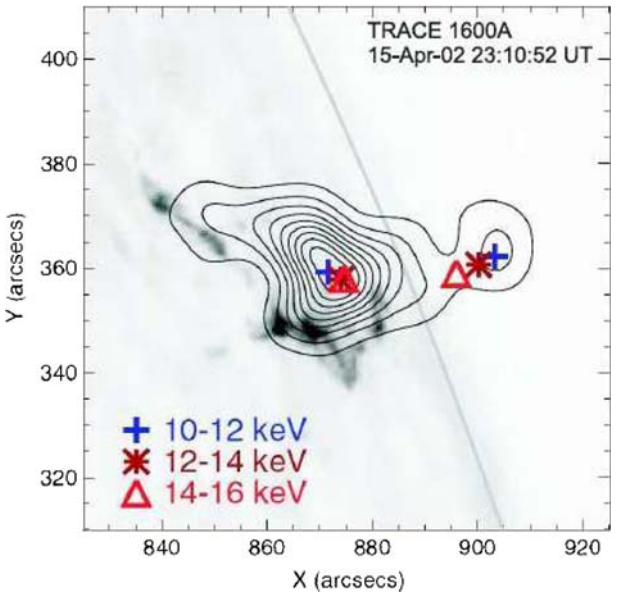

Fig. 3 RHESSI 10–12 keV X-ray image of a flare on 15 April 2002, overlaid on a TRACE 1,600 Å filtergram. The RHESSI image shows thermal emission from the flare loops as well as from a source *above* the loops. The figure shows the emission centroids at three different energies for both the loop-top source and the above-the-loop-top source. The dependence of source height on energy reveals a positive temperature gradient in the lower (loop) source and a negative one in the source above the loops (Sui and Holman 2003)

For one of the Sui–Holman events, SUMER[6] spectroscopic observations were also available (Wang et al. 2007). The SUMER slit nicely crossed the inferred location of the current sheet. The data showed fast bipolar hot plasma flows in locations where Sui et al. inferred the presence of a current sheet, and were thus interpreted as reconnection outflows.

2.2.4 Coronal thick targets

In most flares the observed hard X-radiation comes primarily from the footpoints of magnetic loops (e.g., Duijveman et al. 1982; Sakao 1994), presumably as the thick-target bremsstrahlung of fast electrons stopped in the cold and collisionally dense chromosphere (Brown 1971; Hudson 1972). Now RHESSI observations have revealed a new class of events in which the hard X-ray emission comes predominantly from the coronal flare loop itself, with little or no emission from the footpoints (Veronig and Brown 2004; Sui et al. 2004; Goff et al. 2005; Jiang et al. 2006). We note that SMM[7] and *Yohkoh*/HXT may also have observed events with similar characteristics (Strong et al. 1984; Kosugi et al. 1994). These flares are characterized by steep nonthermal power-law X-ray spectra ($\gamma > 6$) and high column densities ($N > 10^{20}$ cm^{-2}) in the observed soft X-ray flare loops. This column density implies that the corona itself acts as a thick target to the injected electron beam, and thus most of the electrons never reach the chromosphere to produce hard X-ray emission there (Fig. 4). Note that these remarkable flares also have interesting properties at low energies and in the corona above the flaring loops (see also Sect. 2.2.3).

The spectrum in Fig. 4 demonstrates that the emission above ≈20 keV, which is predominantly coronal, is dominated by the (steep) nonthermal power-law component. In order to stop the ≈25 keV electron that could emit this radiation, a mean loop column density of $\approx 10^{20}$ cm^{-2} is needed. Indeed, loop column densities as high as 10^{20} cm^{-2} were inferred from the X-ray data to be present already at the beginning of the events studied by Veronig and Brown (2004), with the densities increasing to several times 10^{20} cm^{-2} later on. In the case of the April 14 flare radio images showed the presence of a hot dense loop at the flare site starting 20 min prior to the impulsive phase (Veronig et al. 2005a; Bone et al. 2007). The corona thus may become sufficiently dense to stop 50 keV electrons.

The enhanced coronal (column) densities observed during solar flares are generally attributed to radiatively unstable "evaporation" of chromospheric matter heated to $>10^5$ K by electron beams or by thermal conduction (Neupert 1968; Hudson and Ohki 1972; Brown 1973; Antiochos and Sturrock 1978). In coronal thick-target events, the electron beam is very efficient in heating the coronal plasma since it deposits most of its energy there and not into the chromosphere. The presence of the dense coronal loops prior to the flare in this case presumably reflects the action of a different mechanism, although the additional coronal heating implied by the coronal hard X-ray emission must indirectly (via conduction) drive additional upward flows.

[6] Solar Ultraviolet Measurements of Emitted Radiation (Wilhelm et al. 1995), on of the instruments on SOHO (the Solar and Heliospheric Observatory, Domingo et al. 1995).

[7] The Solar Maximum Mission (Bohlin et al. 1980).

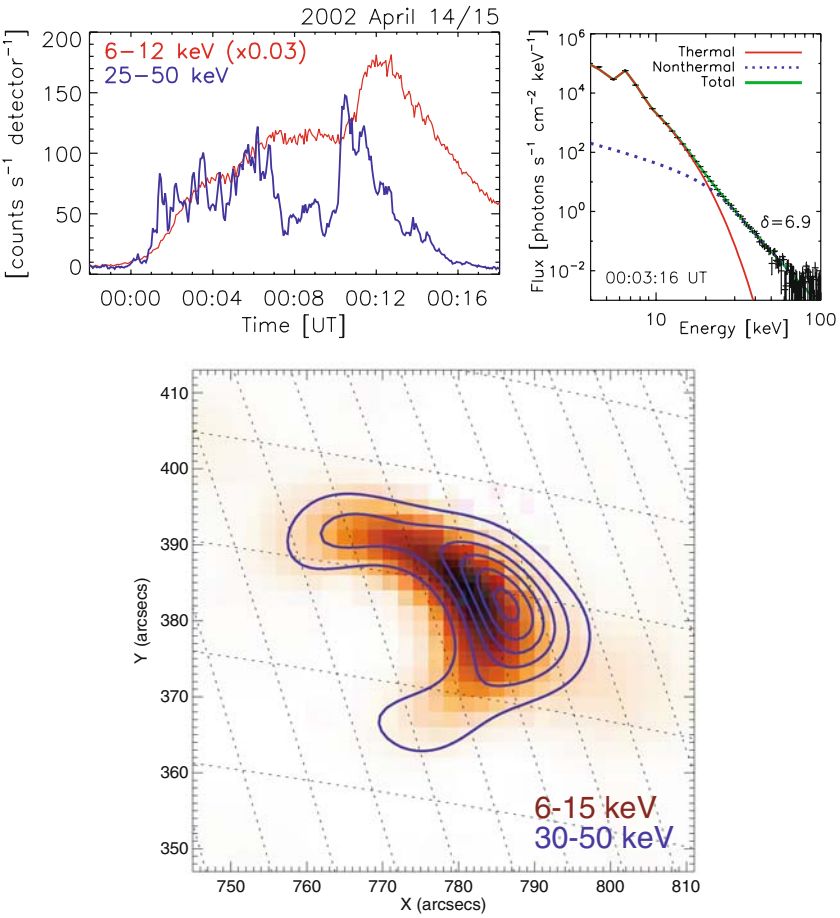

Fig. 4 The coronal thick-target event of 14/15 April 2002 (Veronig and Brown 2004): *Top* RHESSI light curves and spectrum integrated over the burst at approximately 00:03:30 UTC. *Bottom* event-integrated (00:02 to 00:12 UTC) RHESSI image reconstructed using a MEM (maximum entropy method) algorithm. The *color image* shows the 6–15 keV thermal image and the *blue contours* represent the non-thermal emission at 30–50 keV. Contour levels are 20, 35, 50, 65, 80, 95% of the maximum emission. Most of the non-thermal emission comes from the flare loop, with only a hint of emission from the footpoints

2.2.5 Apparent source motions

Sui et al. (2006) identified a special category of flares, called "early impulsive" events, in which thermal emission appearing before the impulsive-phase particle acceleration, usually attributed to pre-flare heating, is minimal. A new type of coronal source motion, along the flare loops and apparently therefore parallel to the magnetic field, has been seen in some of these "early-impulsive" flares. RHESSI 3–6 keV images of a flare on 28 November 2002 are shown in Fig. 5. A coronal source appeared above the limb at the beginning of the flare. As the flare progressed, this source appeared to split into two separate coronal sources moving downward along the flare loop. At the time of the

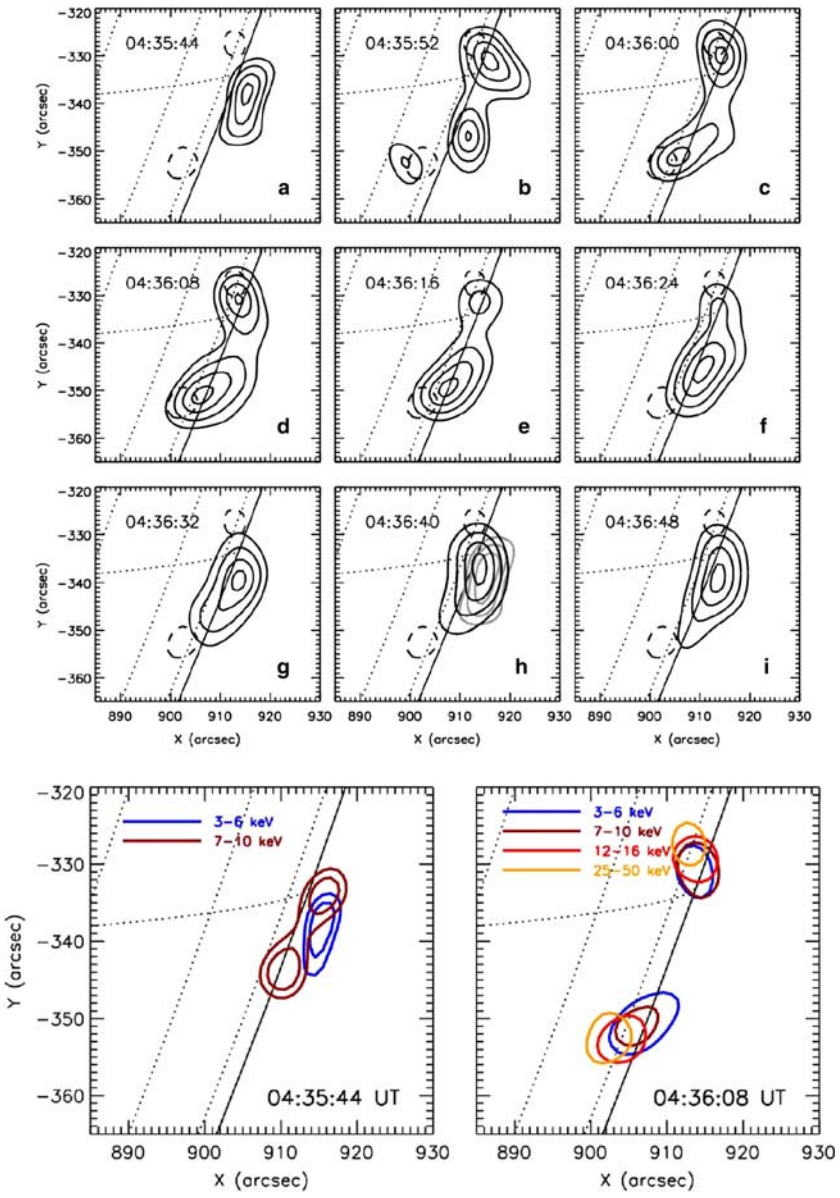

Fig. 5 *Upper* RHESSI 3–6 keV maps of the 28 November 2002 flare, showing the apparent motions upwards along a loop; the 25–50 keV contour image (*dashed contours*) at the hard X-ray peak time is overlaid in each panel. *Lower* images taken at different energy bands show the footpoint locations more clearly. The *solid curves* in all panels show the solar limb, while the *dotted curves* show heliographic parallels and meridians (Sui et al. 2006)

hard X-ray peak, the two sources reached their lowest level, near the footpoints. After that, they moved upwards and eventually settled at the top of the loop. The apparent downward speed was estimated at 500–700 km/s, while the upward speed was only

about 340 km/s. Similar downward and upward motions can also be seen in images at other energies between 6 and 25 keV.

During the period of the downward motion, the higher-energy sources were always located lower than the lower-energy sources (see Fig. 5). Because such an energy distribution is consistent with the thick-target model, which predicts that the high-energy electrons penetrate deeper into the atmosphere before completely losing their energy, Brown et al. (2002) and Sui et al. (2006) suggested that the apparent motion could be caused by the soft-hard-soft electron energy distribution and/or a low-high-low variation of a low-energy cutoff of the electron distribution.

Takakura et al. (1993) had reported similar source motions in hard X-ray events seen with *Yohkoh*/HXT. In four events they found the hard X-ray source to appear at the top of the flare loop, then to spread along the loop toward the footpoints. After the hard X-ray peak, the source became a single source at the looptop. The speed of the source "expansion" ($\approx 10^4$ km/s) would be inconsistent with the sound speed or even the Alfvén speed, but could be explained by "anomalous thermal conductivity." Such source motions may also have been seen with *Hinotori* (Nitta et al. 1990). In one of the two "short but intense" flares these authors describe, which would be an "early impulsive flare" based on our definition, the *Hinotori* 30–60 keV images showed one coronal source apparently split into two separate loop footpoint sources (Fig. 6 of Nitta et al. 1990).

2.2.6 Hard X-ray emission from the high corona and ejections

The partial occultation of a solar flare by the solar limb is an excellent tool for studying faint coronal hard X-ray emissions without competition from the very bright emissions of the footpoint sources (McKenzie 1975; Roy and Datlowe 1975; Hudson 1978; Kane et al. 1979; Hudson et al. 1982). For flares occurring $>20°$ behind the solar limb, not only the hard X-ray footpoints but also the main thermal and non-thermal hard X-ray emissions from the corona are occulted. Flare-related emissions from the high corona ($\approx$200 Mm above flare site) were observed stereoscopically by Kane et al. (1992), associated with a flare occulted by $\approx 40°$ as seen from Earth. Despite this large occultation height, roughly a third of a solar radius, hard X-ray emissions were observed up to 80 keV, with a rather hard spectrum ($\gamma < 3.5$).

Other high coronal events were observed by *Yohkoh* (Fig. 6, from Hudson et al. 2001) as well as by RHESSI (Fig. 7, from Krucker et al. 2007b), so we conclude that high coronal emissions, at least in major flares, are not uncommon. Indeed, Krucker et al. (2007b) found evidence that *all* (8 events total) fast ($v > 1{,}500$ km s^{-1}) farside coronal mass ejections, ie those originating from flares occulted by 20° to 45° (although in a small sample) showed related hard X-ray emissions from the high corona. Multi-spacecraft observations (Kane et al. 1979) had already established that such hard X-ray emissions from the high corona could occur during the impulsive phase of the flare, almost simultaneously with the hard X-ray footpoint emissions. The time profiles of the high coronal events all look similar and show a relatively simple time evolution, with a fast rise and a slower exponential decay. The exponential decay is surprisingly constant, lasting sometimes several minutes without significant deviation, and the photon spectrum exhibits progressive spectral hardening. This might indi-

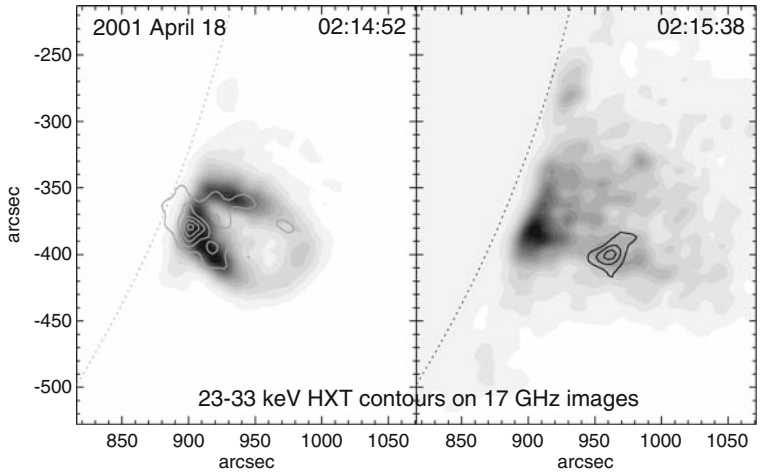

Fig. 6 Contours of hard X-ray emission (*Yohkoh*/HXT M1 channel, 23–33 keV) overlaid on 17 GHz images (Nobeyama radioheliograph) at two different times during the extreme (occultation height of $\sim 100''$) behind-the-limb event of 18 April 2001 (Hudson et al. 2001). In the first image the radio emission outlines a loop, and the hard X-rays are concentrated just above the limb. In the later image the radio emission is much more diffuse and the hard X-rays originate in a more compact source, well above the limb, that coincides with cool filamentary material seen in the 17 GHz images to move outwards at $\approx$1,500 km s^{-1} for over 5 min, out to a height of 1 $R_\odot$ above the limb

cate that mostly collisional losses—without further acceleration—dominate. Density estimates of the ambient plasma support this, as the estimated collisional loss times (Appendix B) of 25 keV electrons have time scales comparable to the event durations. For an early event, the total energy content of the non-thermal electrons in the high corona was estimated at about 0.1% of the total flare energy (Kane et al. 1992). However, the more recent observations suggest that the relative number of energetic electrons (>10 keV) in the high corona may be as large as 10% of the number of thermal electrons (Krucker et al. 2007b). In the event studied by Hudson et al. (2001) the pressure exerted by the non-thermal electrons may have been comparable to that of the core plasma (Figs. 6, 7).

2.3 Late phase

2.3.1 Superhot sources

The so-called superhot sources were discovered via the pioneering balloon-borne observation of Lin et al. (1981), and we include this category here for historical completeness. These observations were the first with high spectral resolution in the hard X-ray range, and they clearly resolved the spectra into two components. One of these was the usual non-thermal component extending to higher energies, and one an exponential type with a characteristic temperature substantially higher than the temperatures obtained from soft X-ray observations, for example with GOES (e.g., Garcia 1994). The qualitative understanding of such sources—which can also be seen as

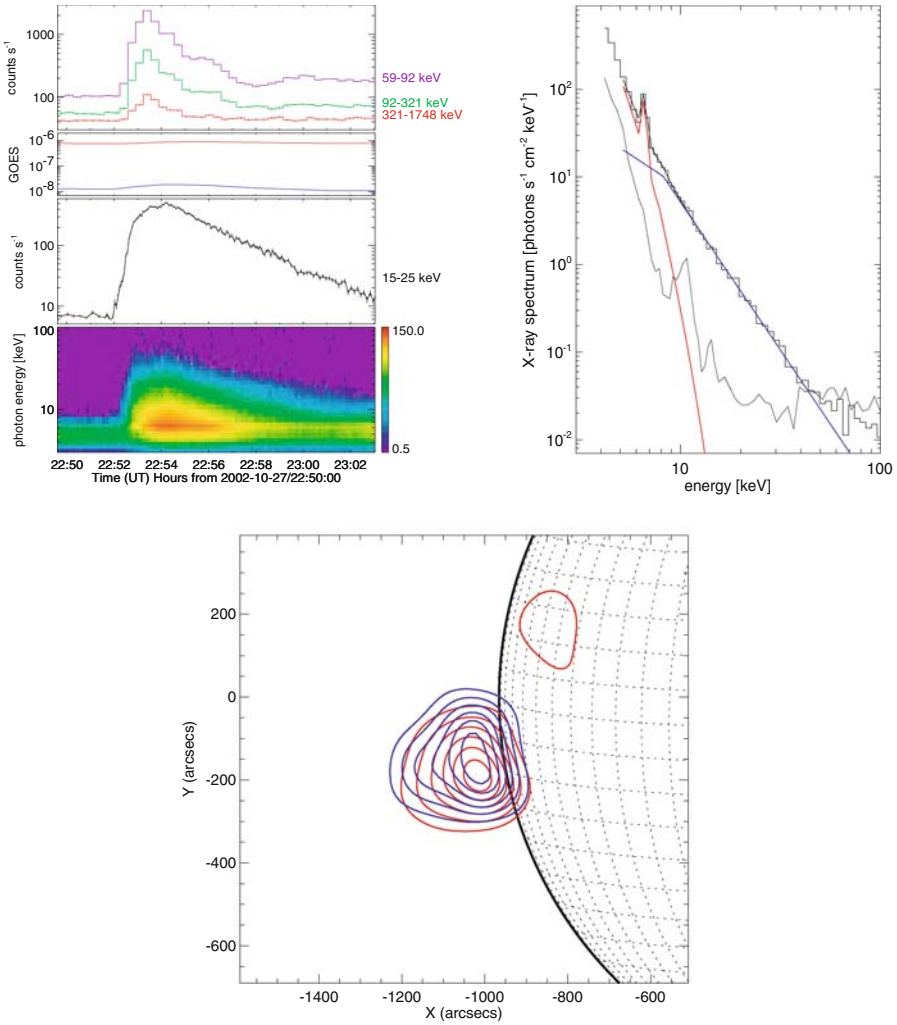

Fig. 7 The 27 October 2002 event (Krucker et al. 2007b). This was seen on-disk from Mars by *Mars Odyssey*, but for Earth-orbiting spacecraft the flare site was occulted by at least 200″ (0.2 $R_\odot$). *Top left* the panels show (1) X-ray and γ-ray time profiles as seen from Mars (the entire flare), (2) the GOES soft X-ray flux (Earth), (3) RHESSI 15-25 keV time profile (Earth), (4) RHESSI hard X-ray spectrogram (Earth). *Top right* the photon spectrum (*black*) during the exponential decay (22:56:48 to 22:57:00 UTC) with the thermal fit in *red* and a broken power law fit in *blue* ($\gamma = 3.4 \pm 0.1$). The *thin gray curve* represents the background emission. *Bottom* RHESSI X-ray imaging in a thermal range (3–7 keV, *red contours*) and a non-thermal range (10–30 keV, *blue contours*) reveals large sources (>200″) seen just above the limb. The RHESSI Clean algorithm was used to reconstruct these images, and the contour levels shown are at 15, 30, 45, 60, 75, and 90% of the maximum. The thermal emission on disk around (−800, 200) is from AR10717 and is already present before the flare occurs

line emission from high-ionization states such as FeXXVI (e.g., Tanaka 1986)—is that they represent the high-temperature tail of the differential emission measure of the collisionally relaxed plasma. The cooling rates are correspondingly faster for such

sources. We are not aware of any systematic RHESSI studies of the superhot sources as such, but the data contain interesting examples (e.g., Holman et al. 2003). Note that the Masuda phenomenon (Sect. 2.2.2) has also been described as a superhot source (Tsuneta et al. 1997; Petrosian et al. 2002), and that such sources may also be closely related to those described in Sect. 2.2.5. Note that in the case of the Masuda flare or others observed only with relatively low-resolution hard X-ray spectrometers, the superhot characteristic spectrum may be confused with the presence of a low-energy cutoff in the electron distribution.

The physical significance of the superhot sources is that they show the highest flare temperatures in plasmas with apparently Maxwellian distributions, and thus may provide clues to the heating mechanism. We note that soft X-ray (e.g. Švestka et al. 1998) and EUV 195Å images (e.g., Warren et al. 1999; Gallagher et al. 2002) often show hot sources, but that such sources should not be termed "superhot" because of their relatively low temperatures. This comment also applies to the hot sources observed in the 195Å channel of EIT or TRACE. This channel has a spectral passband with two maxima, one showing hotter loops (Fe XXI response), usually at higher altitudes, and the other showing loops that have apparently cooled down to more ordinary coronal temperatures (the nominal Fe XI, XII passband; see e.g. Feldman et al. 1999; Warren et al. 1999). Higher structures in arcade flares often have a high-temperature fan extending out into the higher corona (cf. Švestka et al. 1998). Because the hot branch of the TRACE 195Å response is to Fe XXI, it does not show the superhot temperatures if ordinary collisional ionization equilibrium prevails. Imaging in Fe XXVI would be interesting from the superhot point of view. Until then the continuum observations from RHESSI provide the best guide to this phenomenon (e.g., Caspi and Lin 2008).

2.3.2 Gradual late-phase sources

The event of 30 March 1969 (Frost and Dennis 1971) occurred in an active region known circumstantially to have been some distance behind the solar limb (Palmer and Smerd 1972), so that the hard X-rays visible from the Earth-orbiting OSO-5 spacecraft probably originated from relatively high in the corona. Two other examples of quite similar events were reported with OSO-7 data (Hudson 1978; Hudson et al. 1982); such events are characterized by flat hard X-ray spectra (power-law index $\gamma \approx 2$), gradual time profiles, low microwave peak frequencies, anomalously weak soft X-ray emission, and association with coronal radio bursts. RHESSI has now observed sources in this category (see below) but the ten years of *Yohkoh* did not produce a clear example from HXT; we may attribute this to the rarity of such events and to the low image dynamic range of modulation-based imaging instruments. Note too that *Yohkoh* operated with a flare trigger, set normally at a low C-class flare level in the soft X-ray (thermal) range; this biases against detection of limb-occulted events of this type, because the bright low-coronal emissions that normally trigger flare mode are not detected. Without the flare trigger, *Yohkoh* returned only limited (one energy band) hard X-ray data.

Nevertheless a related pattern appears in the so-called "soft-hard-harder" (SHH) spectral evolution of many long-duration hard X-ray events (Cliver et al. 1986; Kiplinger 1995). This spectral pattern differs from the otherwise ubiquitous "soft-

hard-soft" (SHS) pattern associated with the impulsive phase (Parks and Winckler 1969; Hudson and Fárník 2002; Grigis and Benz 2004). From a non-imaging perspective, the hard X-ray spectrum of such a source consists of a gradual, continuously hardening component plus a series of spikes with soft-hard-soft evolution. Often these spikes become more gradual as the event develops, as illustrated in Fig. 8 (and as seen in some of the earliest, non-imaging observations, from the TD-1A spacecraft; see Hoyng et al. 1976).

2.3.3 Coronal sources at MeV energies

Because of its segmented detectors (Smith et al. 2002), RHESSI provides clean imaging above 100 keV, nominally the γ-ray range (e.g., Fig. 9). The rear segments are

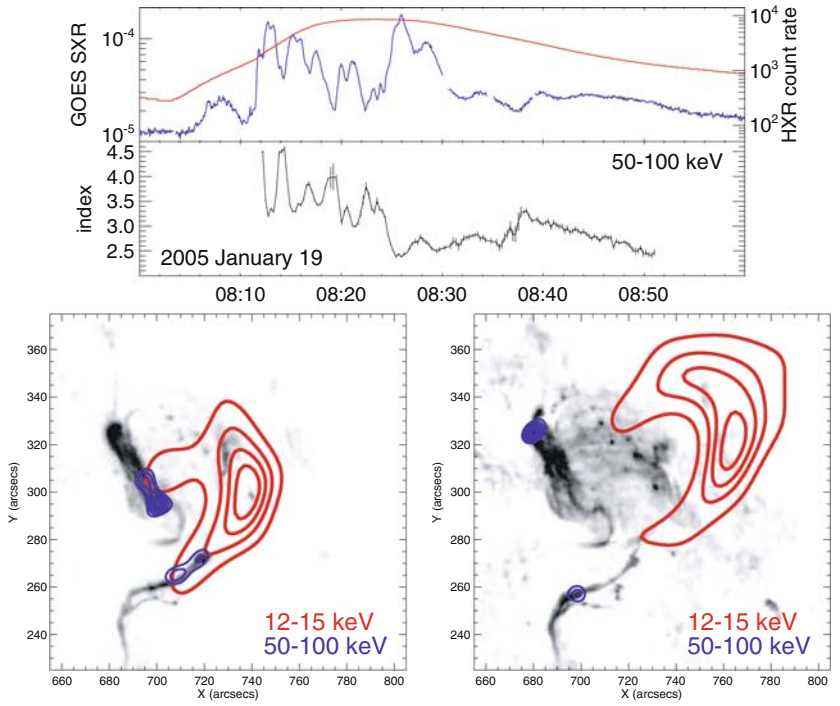

Fig. 8 Hard X-ray spectral evolution and imaging of the 19 January 2005 X-class flare (Saldanha et al. 2008). *Top* the GOES soft X-ray flux (*red*, low energy channel) and RHESSI 50–100 keV hard X-ray (*blue*) count rate are shown in the *top panel*, and the temporal evolution of the power law indices in the energy range between 50 and 100 keV is shown below. Before 08:25 UTC, a soft-hard-soft (SHS) behavior is observed, followed by soft-hard-harder (SHH). *Bottom* hard X-ray imaging results of the 19 January 2005 flare taken during the first hard X-ray peaks (08:11:40 to 08:13:41 UTC, *left*) with SHS behavior and later during the progressively hardening phase (08:43:10 to 08:45:40 UTC, *right*) are presented. Both figures show hard X-ray contours in the thermal (*red contours* are 20, 40, 60, and 80%) and non-thermal (*blue contours* levels 7.5, 15, 30, 50, 70, and 90%) range superposed on TRACE 1,600Å images taken at 08:25:30 UTC (first image available for this flare) and 08:45:03 UTC. For both spectral behaviors, SHS and SHH, non-thermal hard X-ray emissions in the 50–100 keV range are observed from footpoints

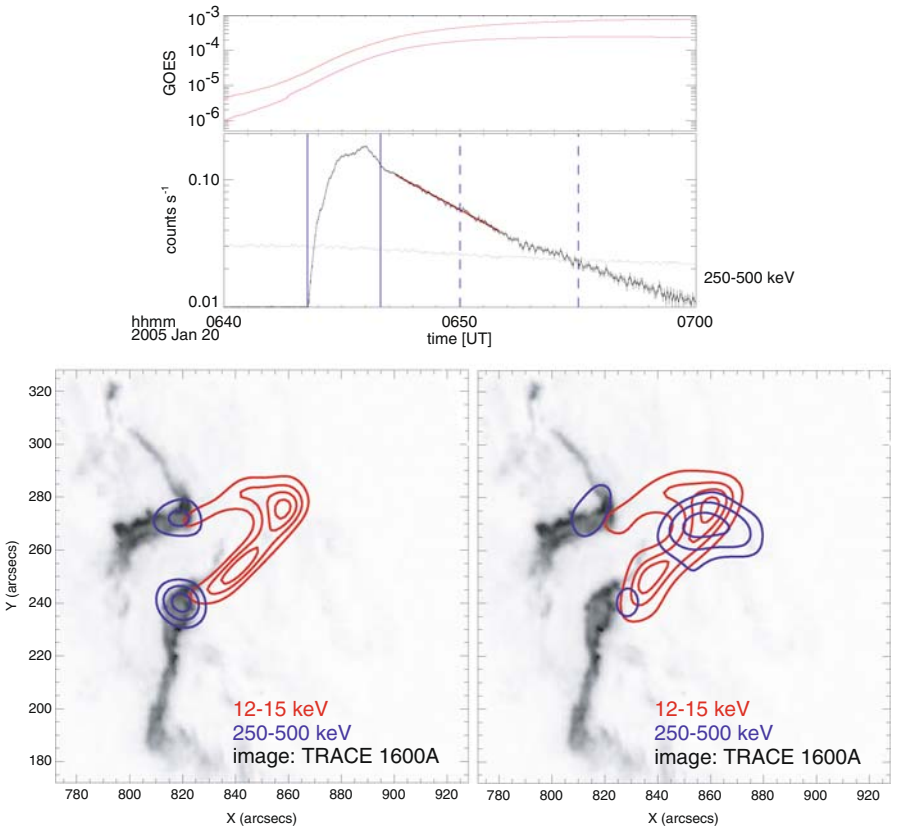

Fig. 9 Time profiles and imaging of January 20, 2005 flare. *Top* the GOES soft X-ray light curve and the RHESSI (rear segment) background-subtracted 250–500 keV time profile (*black*). The *gray curve* shows the RHESSI background rate. The *red line* is an exponential fit to the decay of the hard X-ray peak ($\tau = 257 \pm 2$ s) and the *vertical blue lines* indicate the times of the images shown below. *Bottom left* imaging during the peak time (06:43:32 to 06:46:40 UTC), and during the decay phase (*bottom right*, 06:50:00 to 06:55:01 UTC). Both figures show a TRACE 1,600Å image taken at 06:45:11 UTC overplotted with 12–15 keV (*red*) and 250–500 keV (*blue*) contours. The 12–15 keV image is reconstructed using a MEM algorithm and the contour levels shown are at 30, 50, 70, 90% of the maximum, while the Clean algorithm is used for the reconstruction of 250–500 keV images and 50, 70, 90% contours are displayed. See Hurford et al. (2002) for a discussion of the RHESSI image-synthesis algorithms, including MEM and Clean. During the peak the γ-ray emission comes from footpoints, while later an additional coronal source becomes visible (from Krucker et al. 2008)

shielded from the intense lower-energy fluxes by the front segments of the detectors. This enables high-energy imaging (Hurford et al. 2002) of flares that were seen before only in spectral observations covering both high and low energies. The RHESSI rear-segment observations are limited by counting statistics and dynamic range, so we can produce images in the γ-ray range only for the most energetic events. The three RHESSI flares with best counting statistics in the γ-ray range all show non-thermal emission from their footpoints but all also reveal coronal γ-ray sources

(Krucker et al. 2008). We interpret the emission as relativistic bremsstrahlung, including electron-electron interactions (see Appendix A); technically, therefore, these are really hard X-rays appearing in the γ-ray band.

The coronal sources are most prominent during the exponential decay of the γ-ray continuum and show extremely hard spectra with a power-law slopes between $\approx$1.5 and $\approx$2. The parameters of these coronal γ-ray sources are thus similar to those of the 30 March 1969 archetype (Sect. 2.3; these also showed coronal exponentially decaying emissions with similar intensity and also very hard spectra approaching $\gamma \approx 2$). Such a flat spectral index is close to the hardest theoretically possible bremsstrahlung spectrum, suggesting that the emission is produced by electrons at even higher energies, perhaps a few MeV—there is no strong observational constraint. These observations directly imply that flare-accelerated Mev electrons reside stably in the corona, losing their energy collisionally while also producing γ-ray continuum. The lower-energy electrons scatter and precipitate to the footpoints without losing significant energy in the corona. Hence, the energy dependence of the trapping time should be steeper than for the collisional loss time, and the two loss times should be roughly equal at around $\approx$1 MeV. The observed time scales imply high coronal densities (see Appendix B).

2.4 Surveys

In the following brief sections, for completeness, we describe results obtained from observations prior to RHESSI, some of which may overlap with material presented above. Survey studies of the RHESSI data themselves (e.g., Sect. 2.4.3 below) continue to appear at the time of writing and cannot be dealt with comprehensively yet.

2.4.1 Over-the-limb non-imaging data

Prior to the introduction in 1980 of hard X-ray imaging observations by the HXIS (Hard X-ray Imaging Spectrometer) on board SMM (van Beek et al. 1980), the only knowledge of source height came from a guess about flare longitude and the estimation of an "occultation height" h_{occ} by assuming the hard X-ray-emitting volume to be directly above the flare location radially. Roy and Datlowe (1975) give $h_{occ} \approx R_{\odot}(1 - \sin\theta)/\sin\theta$, where θ is the flare longitude. This means that a flare from an active region one day's rotation beyond the limb would have an occultation height of some 2×10^4 km, a height corresponding roughly to the diameter of a major sunspot. This would isolate a coronal source from a footpoint source, according to then-standard ideas and subsequent imaging observations (Tomczak 2001). As data slowly accumulated for occulted sources observed by this technique (Frost and Dennis 1971; Roy and Datlowe 1975; McKenzie 1975; Hudson 1978; Hudson et al. 1982), it became clear that interesting new physics might be involved. We have discussed observations of sources similar to these in the sections immediately above.

The case-by-case observations of coronal sources from the early non-imaging missions were reviewed by Cliver et al. (1986). This work clearly established a pattern from these scattered events, of which the prototype was the event of 30 March 1969, shown

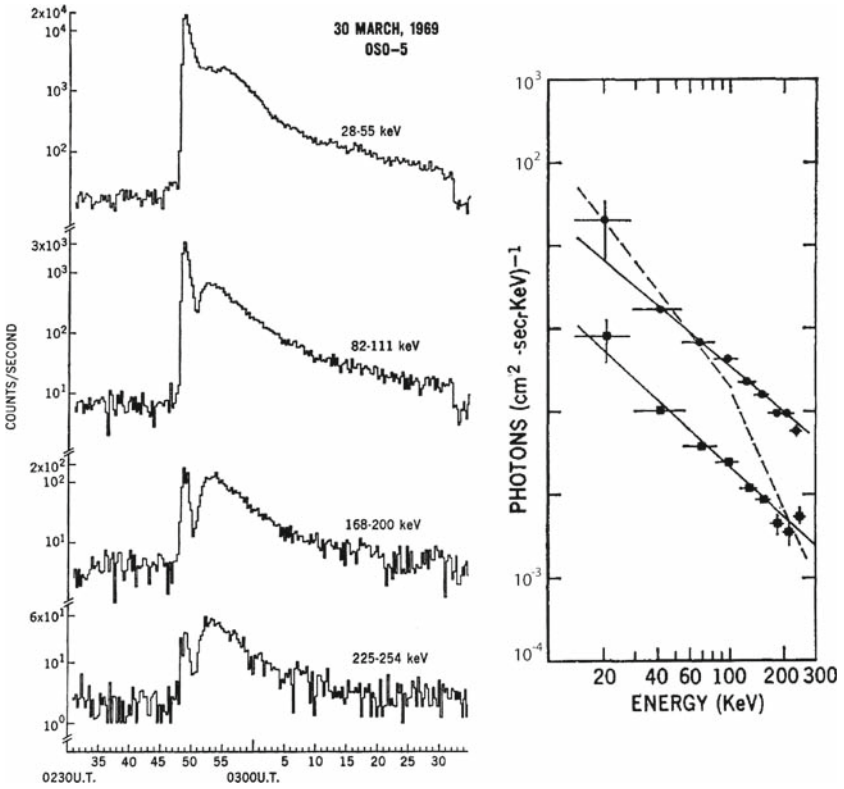

Fig. 10 The "original" coronal hard X-ray event, that of 30 March 1969 (Frost and Dennis 1971) as observed by OSO-5. This enormously energetic event came from an active region behind the limb and produced spectacular radio observations as well (e.g., Palmer and Smerd 1972). *Left* light curves; *right* spectra from the late phase (*top curve* ∼02:52 UTC; *bottom curve* ∼03:07 UTC). The broken power law of the initial burst (*dashed line*) gave way to an extremely flat spectrum in the late phase, approaching a spectral index $\gamma \approx 2$

in Fig. 10. The pattern specifically involved the soft-hard-harder (SHH) morphology of spectral evolution, something sharply distinguishable from the soft-hard-soft (SHS) morphology of the impulsive phase. This type of temporal evolution strongly suggests particle trapping in the solar corona, with the gradual hardening resulting from the erosion of the low-energy region of the velocity distribution function because of collisional energy losses.

A further development was the discovery of a correlation between gradual flare hard X-ray properties and large SEP (Solar Energetic Particle) events (Kiplinger 1995). This was somewhat surprising because SEPs are generally thought to arise via shock acceleration on open field lines much further from the Sun (Kahler 1992; Reames 1999) and thus have no direct relationship with the particles trapped on closed fields in the low corona. We can speculate though that shock physics may be involved in the X-ray sources as well (see Sect. 3.4).

2.4.2 Yohkoh

The HXIS[8] observations from SMM, although they provided the first true hard X-ray imaging, were limited by small effective area and relatively poor high-energy response, with the highest-energy band being 22–30 keV. Accordingly the hard X-ray telescope HXT (Kosugi et al. 1992) on *Yohkoh*—which had four energy channels over a 14–93 keV energy range—really gave us our first systematic view of flare hard X-ray images.

A statistical survey of occulted flares observed by *Yohkoh* revealed the existence of coronal hard X-ray emissions in addition to the main thermal source in most events (Tomczak 2001), but the limited energy resolution of *Yohkoh*/HXT made it difficult to separate these two components unambiguously. The relative source location of the impulsive-phase coronal hard X-ray emission was found to be only slightly displaced ($<6''$) from the thermal soft X-ray emission in all cases except the Masuda flare (Tomczak 2001; Petrosian et al. 2002) (Sect. 2.2.2). A more comprehensive survey (Tomczak M, in preparation) using the mission-long database from the *Yohkoh* HXT Catalogue (Sato et al. 2006) confirms that flares with occulted footpoints have systematically softer spectra than disk flares. Only five occulted flares produced detectable fluxes in the range 53–93 keV, the highest energies imaged by *Yohkoh*/HXT.

2.4.3 RHESSI surveys

The RHESSI observations provide sufficient spectral resolution to separate the main thermal emissions from emissions at higher energies. This can be achieved with the technique of imaging spectroscopy (Hurford et al. 2002). Battaglia and Benz (2006) analyzed five RHESSI flares with coronal sources well separated from the related hard X-ray footpoint emissions, finding also faint hard X-ray emissions with a soft power-law spectrum in the corona in addition to the thermal emissions (Fig. 11). The soft-hard-soft spectral evolution characteristic of the impulsive-phase footpoint sources (Sect. 2.2.1) was systematically found to be present in the associated coronal hard X-ray sources. This strongly suggests that the SHS behavior is intrinsic to the acceleration mechanism itself (Sect. 3.3.4) rather than to the coronal transport.

Statistical results on a large sample of partially occulted RHESSI flares generally confirm these results (Krucker and Lin 2008) as well as those from *Yohkoh* (Tomczak 2001). A coronal hard X-ray source was detected in ≈90% of the 55-event sample, from which Fig. 12 shows a typical event. The coronal component shows time variations in the order of tens of seconds, is most prominent during the rise phase of the thermal emission, and has a much softer spectrum than spectra of comparable on-disk flares. The power-law index is between ≈4 and ≈7, and the centroid position of the source is co-spatial or within a few arcsec of the thermal emission (although for a few events clear separations are observed as well). Interestingly, the difference of ≈2 between the averaged spectral indices of occulted and disk flares is exactly the difference expected between thin- and thick-target bremsstrahlung spectra from a given electron

[8] Hard X-ray Imaging Spectrometer (van Beek et al. 1980)

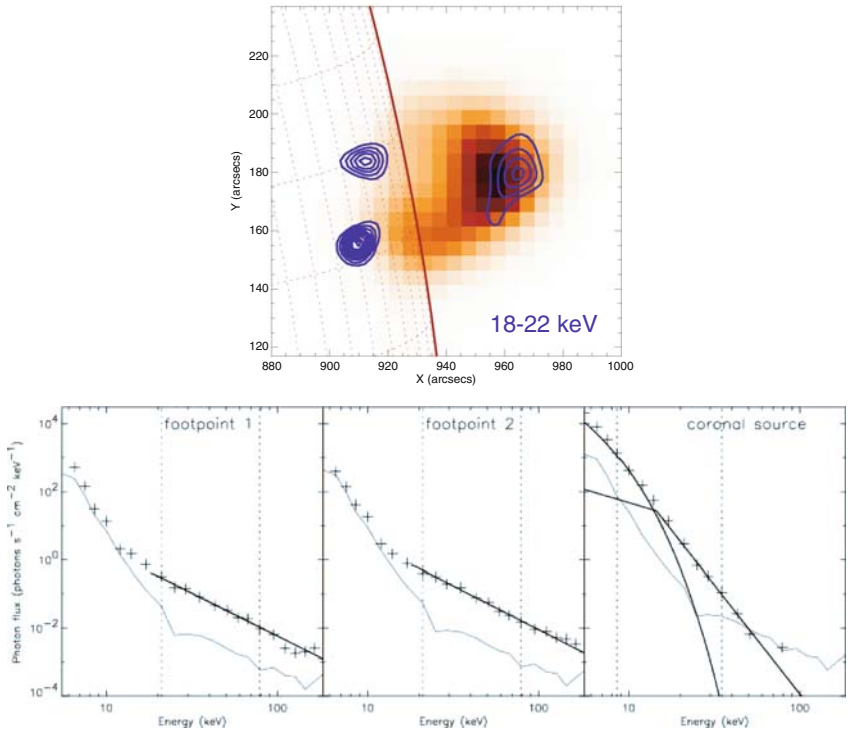

Fig. 11 Imaging spectroscopy with RHESSI. *Upper* the July 13, 2005 flare around 14 UTC, showing coronal emission spatially well separated from the hard X-ray footpoints, making it easy to get spectra for the coronal source and hard X-ray footpoints separately. The RHESSI 18-22 keV contours are averaged over the time period between 14:13:50 and 14:15:48 UTC and overplotted on a GOES SXI image taken at 14:17:05 UTC. *Lower* imaging spectroscopy results from Battaglia and Benz (2006)

distribution (Krucker and Lin 2008). In some events, coronal thin-target emission from flare-accelerated electrons that afterwards lose their energy by collisions in the chromosphere could produce the coronal hard X-ray component (Krucker et al. 2007a). For other events, though, a simple thin-target model does not work (Battaglia and Benz 2007) and non-collisional losses might be important as well.

2.5 Summary of observations

2.5.1 General

The material presented above makes it clear that we can detect coronal hard X-ray emission from all phases of solar flares. The observations reflect non-thermal emissions from electrons over a wide range of energies (few keV for the Sui–Holman "double coronal" type, to MeV for the coronal γ-ray sources) and spatial scales as well. Table 1 summarizes the observations by class of event. The essential observational restriction at present lies in the sensitivity of the observations: solar observations

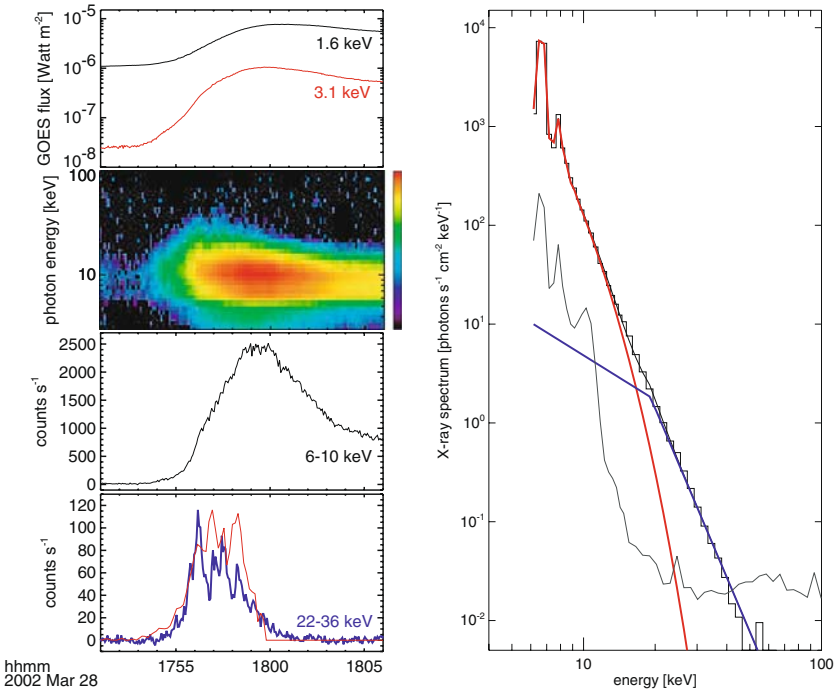

Fig. 12 Typical example of X-ray time profiles and spectrum of a partially disk-occulted flare (Krucker and Lin 2008). From *top* to *bottom*, the panels on the *left* show GOES soft X-ray time profiles, RHESSI spectrogram plot, time profile of the thermal X-ray emission, and time profile at higher energies (*blue*). The panels at the *bottom* additionally show the derivative of the high energy GOES light curve (*red*) in arbitary units. The figure on the right shows the X-ray photon spectrum averaged between 17:55:58 and 17:56:18 UTC with a thermal (*red*, temperature of 24 MK) and non-thermal (*blue*, $\gamma = 5.7 \pm 0.2$) fit. The *gray line* represents the background emission

tend to emphasize bright sources, rather than the faint ones. Thus an enormous range of parameter space remains to be explored.

Table 1 gives rough parameters for as many as ten arguably distinct types of coronal hard X-ray sources, arranged by flare phase of occurrence (pre-impulsive, impulsive, late). Because only a few events have been identified in some categories (for example, only two "fast ejecta" events have been described) we do not want to use Table 1 as a classification scheme, but rather just to illustrate the breadth of the observational material and its potential. The reference line at the bottom of the table represents the standard "footpoint" sources, for which the archetype event is that observed by Hoyng et al. from the Solar Maximum Mission (Hoyng et al. 1981). All hard X-ray flares except for the "coronal thick target" category seem to show this type of emission, and there are several examples (such as that of Fig. 8) illustrated in this paper.

The novelty of the coronal hard X-ray observations seems to lie in two major areas: phenomena appearing in the lower corona before or during the impulsive phase (Sects. 2.1, 2.2.3 and 2.2.4); and phenomena in the middle corona mainly in later phases. The former category began with the Masuda event, which apparently was an extreme example of the kinds of phenomena RHESSI is now showing more clearly: the

appearance of a current sheet or a "coronal double source." It is clear the coronal hard X-ray observations in either category generally do not require high spatial resolution, but do require sensitivity and image dynamic range, and in some cases an imaging field of view[9] larger than RHESSI's.

The coronal sources, spread out over the different flare phases, probably involve different physics from the standard thick-target model that fits the impulsive phase well enough. For that reason the theoretical discussion following immediately in Sect. 3 should be viewed as a first serious attempt to deal with some heretofore unexplored problems. We suggest that non-solar hard X-ray sources (e.g., stellar flares), to the extent that the thick-target scenario does not work, might find alternative analogs here.

2.5.2 Coronal mass ejections

The detection of hard X-ray emission from high altitudes opens a new domain for interpretation, emphasizing open (or opening) fields, ejecta, and large-scale shock waves instead of the usual machinery of the impulsive phase, observed mainly in or near the chromosphere. Although this is the domain of meter-wave radio astronomy, and there is a rich history of observations (e.g., Wild et al. 1963; Kundu 1965; Bastian et al. 1998), there is little multi-wavelength literature yet on these phenomena. In general the SOHO observations (especially LASCO[10]) give a general view of associations but do not have sufficient time resolution to be of much use in detailed analysis. Further, the hard X-ray imaging of the coronal sources has just begun, with RHESSI, and is strikingly limited by several factors—sensitivity, image dynamic range, and imaging field of view. We note that the fraction of flare energy that eventually appears in particles accelerated by the CME-driven shock may be large (of order 10%; see Emslie et al. 2005; Mewaldt et al. 2005). These particles can certainly contribute to the radiation signatures, but probably on longer time scales and large spatial scales. Kahler and Ragot (2008) discuss the possible remote-sensing signatures, which conceivably even include mechanisms involving interplanetary dust particles.

3 Theory

3.1 Introduction

The previous section has outlined the wide range of coronal hard X-ray sources (Table 1), demonstrating that the morphologies differ enough from the standard thick-target model to encourage a reconsideration of theories for particle acceleration and transport in flares. In Appendix A we revisit the theory of continuum emission mechanisms, and suggest that mechanisms other than bremsstrahlung could play a role in the coronal sources, but for the remainder of the discussion here we retain the nor-

[9] RHESSI has full-Sun coverage, but an imaging field of view within this that is limited by its coarsest modulation collimator at 183.25″.

[10] The Large Angle Spectroscopic COronagraph (Brueckner et al. 1995).

mal assumption that bremsstrahlung dominates. In this we follow Korchak's definitive early work on the emission physics (Korchak 1967, 1971).

Interpretations of (coronal) hard X-ray sources may be divided, roughly speaking, into two classes. The first class starts out by concentrating on properties of hard X-ray sources produced only by transport effects (e.g. binary collisions, magnetic mirroring), leaving the acceleration to a coronal "black box." Any properties of coronal sources not accounted for in these terms constitute clues to the character of the electron acceleration mechanism. This is the style of the classical thick-target theory (Brown 1971; Hudson 1972). Alternatively one may attempt to include acceleration physics—possibly self-consistently with the electron transport—from the outset. In practice many acceleration models pay little attention to the geometry of the corona in which the sources are formed, whereas those utilizing a "black box" accelerator and focusing on transport can take account of the source environment in some detail. Thus each approach has something to offer.

The particle acceleration process(es) present a formidable difficulty, particularly if one seeks to explain the inferred flux of electrons giving rise to the chromospheric hard X-ray sources - and it is common to assume that the electrons producing the coronal source are part of the same initial population, with a fraction propagating downwards to reach the chromosphere and a fraction radiating in the corona. We note here that recent results from RHESSI (Kontar and Brown 2006; Kašparová et al. 2007) suggest that the chromospheric sources are not consistent with production by a downward-directed particle distribution from the corona, and the coronal and chromospheric electron populations may yet be unrelated, with an agent other than particles transferring the bulk of the flare energy to the chromosphere (e.g., Fletcher and Hudson 2008). In that case, explaining only the coronal-source electron acceleration could prove less challenging.

A range of different acceleration mechanisms has been proposed over the years (see Miller et al. 1997 for a review up to the mid-1990s and Aschwanden 2002, for more recent developments). For closed coronal regions, possible processes include stochastic acceleration by MHD turbulence, either fast or Alfvénic: (e.g., Miller and Ramaty 1987; Miller and Roberts 1995; Miller 1997; Hamilton and Petrosian 1992; Petrosian and Liu 2004) or stochastic current sheets (Turkmani et al. 2005, 2006); acceleration by strongly electric fields above the Dreicer limit (Dreicer 1959) in an electrostatic double layer (Alfvén and Carlqvist 1967) or in the close neighbourhood of a reconnecting structure (e.g. Martens and Young 1990; Litvinenko and Somov 1993; Dalla and Browning 2005; Zharkova and Gordovskyy 2005; Litvinenko 2006); or perhaps by relatively strong shock waves (e.g. Lee and Ryan 1986; Blackman and Field 1994; Tsuneta and Naito 1998; Mann et al. 2006). In Sect. 3.3 we focus on the acceleration mechanisms. First we consider interpretations of coronal hard X-rays relying primarily on transport, recalling some basic observational properties of the sources.

3.1.1 Target conditions and thin-target coronal sources

Electrons traversing some region of the atmosphere radiate via bremsstrahlung in close encounters with ambient particles. If they leave this region with energies essentially

unchanged we are dealing with a "thin target" situation. If, at the other extreme, they stop completely in the region we have a "thick target" and need to account for the evolution of their energy distribution as they slow down. A coronal volume that is a thick target to low-energy electrons could be thin at higher energies, depending on whether the electrons escape that region or are trapped. These definitions assume that emitting particles interact almost always with ambient plasma particles in the region which they traverse, i.e. that they are "dilute." In "thermal" models, on the other hand, all electrons in the source region have comparable energies and have had time to attain a relaxed, Maxwellian distribution.

Consider a simple flare loop of uniform density and uniform magnetic field strength, and an accelerator that injects electrons at some point along the loop length (as opposed to one which operates throughout the loop volume). If we disregard any form of coronal confinement, so that the electron only has a single pass through the corona before encountering the chromosphere and being collisionally lost, then typical coronal densities will present thin targets to all but the lowest energy electrons. For example, a coronal loop of length 10^9 cm and density 10^{10} cm^{-3} is collisionally thin to electrons above about 8 keV. The observed instantaneous flux of photons from a thin-target region is simply related to the fast electron distribution [(6) in the Appendix].

In this thin-target scenario, without any modification of the energy spectrum, steady acceleration will result in an instantaneous coronal density of accelerated particles that is spatially uniform at all energies. A coronal source could appear due to line-of-sight effects, with an enhancement factor depending only on the emitting column along the line of sight. This could be large for e.g. a loop observed end-on (in its plane) near the limb. However, looking down on a loop on the disk would tend to result in loop legs being enhanced. This geometrical enhancement would be the same at all energies produced by the thin-target electrons (assuming all energies are optically thin). See Alexander and Katsev (1996) for a related discussion for optically thin, uniform soft X-ray emission.

A time-varying accelerator in a thin-target loop could produce concentrated sources if the observational integration time were less than the electron transit time along the loop, and velocity dispersion could give a source appearance that changes with energy or time (e.g., Aschwanden et al. 1996, 1999). However, given that typical integration times for both *Yohkoh* and RHESSI sources of hard X-rays are seconds, this is unlikely to be the case. There is also no reason why this would produce sources preferentially concentrated around the looptop.

The relatively high looptop-to-footpoint intensity ratio is also problematic for a coronal thin target. At a given photon energy ϵ this ratio would be roughly equal to the coronal line-of-sight column depth divided by the chromospheric stopping column depth (see Sect. 3.1.2) of an electron at 2ϵ (i.e. producing photons of energy ϵ), and this will typically be very small. For example, a 40 keV electron producing $\approx$20 keV photons decelerates collisionally over a stopping column depth of $\approx 10^{20}$ cm^{-2}, producing far more photons than a coronal source of (high) density 10^{10} cm^{-3} and length of perhaps 10^9 cm.

It seems clear that a bright, concentrated, looptop coronal hard X-ray source cannot be formed in a coronal thin target. It is necessary to modify the environment in which the electrons move and radiate and/or their spatial and angular distribution, in

such a way as to increase their radiation yield at the loop apex compared to the footpoints; see the beginning of Petrosian and Donaghy (1999) for a related discussion. In what follows, we consider coronal confinement by collisional, magnetic and turbulent mechanisms.

3.1.2 Collisional transport

In a fully ionised hydrogen plasma, a non-relativistic electron of initial energy E (keV) stops completely in a column depth $N_s(E)$ (e.g., Emslie, 1978):

$$N_s(E) \;=\; 1.5 \times 10^{17}\mathrm{cm}^{-2}\;(E/\mathrm{keV})^2 \tag{1}$$

If the coronal portion of a loop has column depth N, hard X-ray sources will thus change morphology from coronal to footpoint at a photon energy of approximately $\epsilon_s = \left(N/1.5 \times 10^{17}\right)^{1/2}$ keV. As seen above (Sect. 2.2.4), coronal densities can sometimes be great enough to make ϵ_s as large as 60 keV. However such cases are not the norm. This simple collisional hard X-ray morphology cannot always account for bright, isolated coronal sources.

The above assumes uniform or at most smoothly varying coronal loop density; however, Feldman et al. (1994), suggested from soft X-ray observations that the flaring corona might include localised regions of greatly enhanced density ($\approx 10^{12}$ cm^{-3}). Wheatland and Melrose (1995) applied this observation to explain the observed Masuda coronal hard X-ray source. The coronal portion of a loop is still characterised by a column depth N and hard X-ray morphology with a transition at photon energy $\epsilon_s(N)$, but most of this N is now represented by a region near the top of the loop. Battaglia and Benz (2007) confront this model with RHESSI observations of coronal hard X-ray sources but find that it fails in several respects.

Fletcher (1995) suggested that the time during which electrons remain and radiate in the corona can be enhanced by having a somewhat enhanced coronal density (on the order of a few times $10^{10}\mathrm{cm}^{-3}$) and an isotropic (or "pancake") rather than forward-beamed electron distribution, so that the fraction of particles injected at high angles to the magnetic field do not progress quickly down the loop but spend a longer fraction of their radiating lifetime in the corona compared to particles with a small pitch angle. A pancake type distribution in turn might result if electrons in the coronal source are accelerated by intense electromagnetic radiation produced via the Electron Cyclotron Maser (Sprangle and Vlahos 1983) occurring on the field lines where the primary flare energy release actually takes place (Conway and MacKinnon 1998). This picture could also account for the displacement of the Masuda source from the flare thermal loop.

For any assumed coronal density profile, with or without condensations, we can model collisional electron transport and calculate the resulting hard X-ray energy-dependent spatial structure. Ideally Fokker–Planck (e.g., Leach and Petrosian 1983) or Monte Carlo (e.g., Bai 1982) methods are used, correctly treating pitch-angle scattering. Prior to hard X-ray imaging, results from such efforts were compared with multi-spacecraft observations of partly occulted flares (Kane 1983). On some occasions theory and modelling are straightforwardly consistent and yield plausible esti-

mates of coronal density. Other events, however, need either implausibly high coronal densities or containment of electrons in the corona (Leach and Petrosian 1981; Brown et al. 1983).

3.2 Particles in coronal magnetic flux tubes

3.2.1 Coronal trapping

Progressive spectral hardening in extended hard X-ray bursts (Frost and Dennis 1971; Hudson 1978; Cliver et al. 1986; Kiplinger 1995) has been interpreted in terms of coronally trapped electrons (Ramaty 1979; Bai and Ramaty 1979; Vilmer et al. 1982). The collisional energy loss time of a (non-relativistic) electron of energy E (keV) is given by (e.g., Vilmer et al. 1982, see also Appendix B):

$$\tau(E) = A \frac{E^{3/2}}{n_e}, \tag{2}$$

where n_e is the electron number density and A $= 2 \times 10^8$ s kev$^{-1.5}$ cm^{-3}. The longer lifetimes of higher energy electrons result in progressive spectral hardening, on timescales of order 100–1,000 s for plausible coronal densities. As a result, the progressively hardening X-ray sources have been viewed as "coronal" emission, even when no spatial information exists. One assumes in these models that electrons are accelerated early in the burst and that their later evolution is determined entirely by energy loss in the coronal trap: the accelerator is assumed to give them high energies effectively instantaneously but to play no further role in their evolution. Whether this is physically realistic or not, such modelling can often reproduce the observed temporal evolution in detail (Vilmer et al. 1982; Dauphin and Vilmer 2007). These models now need to be expanded in scope to incorporate RHESSI imaging spectroscopy (e.g., Emslie et al. 2003) and simultaneously microwave imaging spectroscopy (e.g., Hurford et al. 1984) as well.

3.2.2 Precipitation

Let B_0 and B_1 denote the minimum and maximum values of magnetic field strength in the coronal portion of a loop, B_1 presumably applying at the loop footpoints. An electron is trapped in the corona if the angle θ between its velocity vector and the magnetic field satisfies

$$\sin^2\theta \geq \sin^2\theta_0 = \frac{B_0}{B_1}. \tag{3}$$

Quiescent active region loops viewed in soft X-rays or UV often show constant cross-sections (e.g., Klimchuk 2000; Watko and Klimchuk 2000) and this sort of trapping seems most relevant either to large heights, where dipole-like fields predominate, or

to field structures in the vicinity of a current sheet or magnetic null (e.g., Fletcher and Martens 1998; Giuliani et al. 2005)

Pitch-angle scattering means trapping is never perfect. Three qualitative regimes of scattering and escape in magnetic bottles may be identified: weak, moderate and strong. The first two were identified by Kennel and Petschek (1966) and Kennel (1969). We summarize their properties in Table 2, in terms of loop transit (τ_l) and pitch-angle scattering (τ_s) times, the loop length L and the spatial diffusion coefficient D. Electrons radiate their thick target yield effectively instantaneously on precipitation and the relationship between the coronal and footpoint fluxes, as a function of energy, follows in each of these regimes from the escape times of Table 2. Binary collisional scattering necessarily takes place in the weak limit; otherwise the similarity of energy loss and scattering times means that we have a coronal thick target. Detailed modelling, capable of comparison with observations, has been carried out for collisions (Melrose and Brown 1976; MacKinnon 1988, 1991; McClements 1990) (also by for microwave source modelling Lee and Gary 2000) and for wave-particle interactions (Trottet and Vilmer 1984; Stepanov and Tsap 2002). Coronal sources in weak and moderate cases are necessarily diffuse, on the scale of the loop, although their flux and spectral distribution compared to the related footpoint sources will vary depending on the energy-dependent scattering rate and gross parameters of the loop (length, mirror ratio). The presence of footpoints does not mean that no coronal trapping occurs: the total coronal flux may be greater or less than the total footpoint flux, the coronal X-ray emission may be spread over several pixels and overall spectral hardening will still result (MacKinnon 1991).

Numerical modelling of trap plus precipitation in a converging magnetic field was carried out by (Leach and Petrosian 1981, 1983) who predicted the existence of coronal sources formed in this way, particularly at low energies and in strongly convergent magnetic fields, illustrating what may be possible in magnetic geometries more elaborate than single loops. Fletcher and Martens (1998) produced coronal sources from forward-beamed electron injection in a magnetic geometry such as might be found below a coronal current sheet (see Sect. 3.3.2). Both models predict softer coronal than footpoint spectra, a combination of collisionally thick- and thin-target behaviors. Fletcher and Martens (1998) predict sources that are more compact at high energies.

In the strong limit, turbulence excited by the particles themselves scatters them so rapidly that they are once again effectively contained in the corona (Trakhtengerts 1984; Bespalov et al. 1987), albeit between two turbulent regions that travel along the loop at the group velocity of the turbulent wave mode. Such a situation can in principle account for isolated coronal sources. Stepanov et al. (2007) claim that strong scattering of electrons by whistlers can account for the observed evolution of a 17 GHz radio source on 27 August 1999; an expanding coronal hard X-ray source would

Table 2 Escape time τ_{esc} versus scattering "depth" τ_l/τ_s

	τ_l/τ_s	τ_{esc}
Weak	$\ll 1$	τ_s
Moderate	≥ 1	$\tau_l\,(1-\cos\theta_0)$
Strong	$\gg 1$	L^2/D

presumably have accompanied this event, had spatially resolved observations been available. Énomé and Tanaka (1971) had suggested an (ad hoc) turbulent confinement for the "original" coronal hard X-ray source illustrated in Fig. 10.

3.3 Acceleration mechanisms

3.3.1 The "standard model" and acceleration

Up to this stage, we have discussed the confinement and emission processes for hard X-ray-producing electrons under the assumption that electron acceleration happens through an unspecified process. It is now appropriate to return to the question of acceleration per se, particularly in the context of coronal geometries that can (a) accelerate particles and (b) confine them.

A consequence of the great attention given to the *Yohkoh* coronal hard X-ray sources (especially the Masuda flare) has been the suggestion of a standard or even "unified" model of flares (Shibata 1996). Based on the evidence of the above-the-loop-top hard X-ray source (Masuda et al. 1994) described in Sect. 2.2.2, hypothetically associated with a reconnection exhaust jet (Shibata et al. 1995). These observations all seem consistent with the scenario of the standard reconnection model: (1) a stressed coronal magnetic field becomes destabilized, leading to macroscopic reconnection associated with the ejection of a plasmoid (a flux rope in 3D); (2) this ejection induces an inflow which constitutes the main driven phase of the flare; (3) the exhaust jet from the reconnection leads to shock formation, plasma heating and particle acceleration. Note that this is a 2D scenario.

The origin of this model lies in the theories of large, eruptive flares developed since the mid-1960s which involved a rising coronal reconnection site and associated soft X-ray emission during the flare decay phase (e.g., Sturrock 1966; Hirayama 1974; Kopp and Pneuman 1976; Heyvaerts et al. 1977; Cargill and Priest 1983). It is unclear whether it can be extended to the impulsive phase. It should also be stressed that this standard model—a framework for discussion, rather than a quantitatively successful theory—does not address particle acceleration issues, especially the high efficiencies required if seeking to explain the hard X-ray footpoints by electrons accelerated in the corona. The standard model places the particle acceleration is in a region of (a) relatively low plasma density, hence amplifying the number problem (Brown and Melrose 1977; Fletcher et al. 2007) associated with the intense footpoint emission and its associated electromagnetic complexities with respect to particle beams, and (b) in a region most likely having weaker magnetic field. Alternative scenarios are presented below.

It should nevertheless also be noted that macro- (and meso-) scale reconnection sites do present excellent opportunities for particle acceleration through direct electric fields (e.g., Litvinenko and Somov 1993) or turbulence associated with the reconnection outflows and (perhaps) shock waves. Although this is the framework Litvinenko and Somov (1993) adopt, the single monolithic current sheet of the standard model may not be a proper description. Current sheets over a wide range of scales might have the property of efficient particle acceleration. Indeed the representative cartoon of

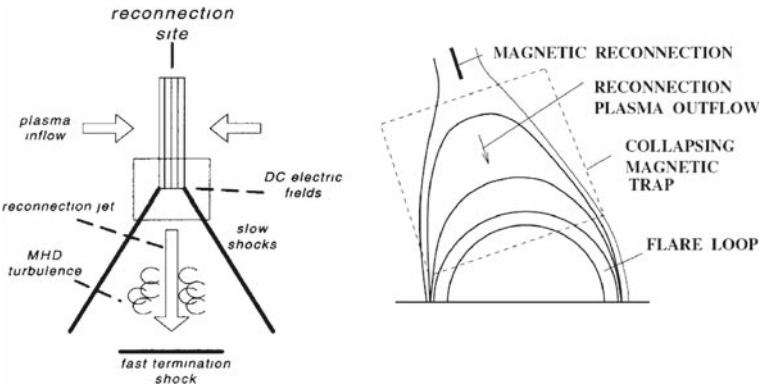

Fig. 13 *Left* cartoon showing the current sheet and associated processes invoked as the core of the standard model (Cargill 2001). However, such processes can occur at current sheets with a wide range of scales. In particular island formation, as illustrated in Fig. 15, could take place within the current sheet. *Right* a sketch of the collapsing magnetic trap (Karlický and Kosugi 2004)

Fig. 13 (left) illustrates these possibilities without specifying where the current sheet occurs or how large it is.

3.3.2 Collapsing traps

The proposed magnetic geometry in the standard model does have some attractive features for coronal hard X-ray sources. This has led to the "collapsing trap" model as sketched in Fig. 13 (right). We discussed observations relevant to this process, including source motions that could be interpreted as collapse or implosion, in Sect. 2.1.

As noted above, the standard model envisions an exhaust jet in which field lines become shorter with time at a fraction of the Alfvén speed. It can be argued that this decrease of field volume quite generally corresponds to the release of stored magnetic energy (Hudson 2000). The resulting collapsing magnetic field (Svestka et al. 1987; Forbes and Acton 1996) could capture pre-accelerated particles escaping from the current sheet and accelerate them further inside the trap, either by the betatron mechanism (Brown and Hoyng 1975) or also by Fermi acceleration between the slow shocks associated with the current sheet (Somov and Kosugi 1997; Karlický and Kosugi 2004; Bogachev and Somov 2007). A typical magnetic trap will collapse in a few seconds during which time the particles scattering from the approaching mirrors will undergo several crossings of the loop. The pre-acceleration could occur in turbulence within the current sheet, or by the convective electric field itself (Speiser and Lyons 1984; Litvinenko and Somov 1993) albeit for a rather small number of particles due to the small size of the non-adiabatic region around the current sheet. A more general development of turbulence (see Sect. 3.3.5) could in principle greatly increase this number.

Acceleration in a collapsing trap is due to the betatron mechanism (based on the conservation of the first adiabatic invariant) and the Fermi mechanism (as the magnetic trap length shrinks) therefore unless the change of the magnetic field strength in the

collapse is large, the energy gain due to collapse is modest. Acceleration efficiency is limited by the tradeoff between betatron gains, collisional losses, and detrapping because the loss-cone increases in size due to the increasing ratio of coronal to chromospheric field strength. Somov and Bogachev (2003); Bogachev and Somov (2007) claim that this last effect exactly balances the betatron increase, so that the Fermi mechanism is the important one in providing the net increase. This result is apparently not borne out by the numerical simulations of Karlický and Kosugi (2004) who follow test particles collisionally scattering and accelerating within a magnetic field described by a simple analytic model in which the field strength increases but the loop length remains constant. In their model, electrons with high pitch angles (further increased by the betatron process) accumulate around the low field region at the loop midpoint. They find that for trap densities around 10^{10} cm^{-3}, and a magnetic field increasing by a factor 10 in 4 s, electrons above about 5 keV injected energy are accelerated to tens of keV. Lower trap densities will require correspondingly lower initial energies.

Subsequently, Karlický and Bárta (2006) used a 2D MHD code to analyze the outflows from a current sheet and then follow test particles injected inside the collapsing magnetic structures. An additional acceleration due to Fermi acceleration is present. Giuliani et al. (2005) have analysed particle dynamics in a collapsing trap including a guide field (i.e. out of the plane in Fig. 13), finding that electrons not only mirror in the collapsing traps but also drift, which may play a significant role in the energetics, depending on the overall magnetic topology in the vicinity of the collapsing trap. However, the energy gain is still limited by the change in the field magnitude during collapse. Overall, to obtain tens of keV electron energy in a collapsing trap, from an initial thermal distribution at $T_e \lesssim 1$ keV, requires a field strength that increases by a factor of 100 or so. This may be possible in the reconnecting field very close to a magnetic null, or in a rapid collapse from a very stretched-out initial magnetic configuration with reconnection occurring high in the corona. Finally, multiple Fermi accelerations in a turbulent collapse could also lead to the higher energies (Sect. 3.3.5).

It is clear that these "collapsing trap" ideas may be relevant for coronal hard X-ray sources on large scales (the gradual phase) as well as for the impulsive phase. The launching of a coronal mass ejection (CME) involves the expansion of coronal magnetic field into interplanetary space, and this ultimately requires a pinching-off with sunward flows in order to preserve the interplanetary field at its approximately constant value (Gold 1962; McComas et al. 1992). Motions similar to those implied by this picture can be seen in soft X-rays (McKenzie and Hudson 1999), EUV (Gallagher et al. 2002; Sheeley et al. 2004), and possibly even in white light (Sheeley et al. 2004) as well.

3.3.3 Weak turbulence within a flaring loop

We now discuss alternative scenarios for particle acceleration and confinement in flares. We discuss mainly how imposed "weak" turbulence accelerates, scatters and confines particles, returning to a discussion of the origin of the turbulence in Sect. 3.3.5.

If plasma turbulence is present in the corona throughout a large coronal volume, it can both accelerate and trap particles. In such cases, the accelerator is co-spatial with the coronal hard X-ray source. Electron acceleration by plasma turbulence has been

studied by several authors, and in the solar literature two main processes have been identified: stochastic resonant acceleration by a spectrum of high-frequency plasma turbulence (e.g., Miller and Ramaty 1987; Hamilton and Petrosian 1992), and transit time damping by lower frequency turbulence (e.g. Miller 1997; Lenters and Miller 1998). The waves are assumed to introduce a scattering length which is much smaller than the Coulomb scattering length which, at low energies, is comparable to the Coulomb energy-loss length. Electrons thus undergo many pitch angle scatterings before losing substantial energy. If the wave scattering length is smaller then the loop length, the energetic electron distribution will be isotropized, or form other pitch-angle distributions (e.g. pancake-type) and the emission at the top of the loop will be enhanced. Thus the electrons can be both energised and inhibited in their motion along the magnetic field.

Under the assumption of weak scattering, the evolution of the distribution function f in position s, time t and energy E, under the influence of scattering, energy loss and systematic acceleration can be modeled using a kinetic equation. Further assuming that the scattering that is efficient and can isotropize the electrons on a timescale shorter than either the acceleration time or the energy loss time means that only the diffusion in energy space need be considered. The appropriate equation is then:

$$\frac{\partial f}{\partial t} = \frac{\partial^2}{\partial E^2}[D(E)f] - \frac{\partial}{\partial E}[(A(E) - \mid \dot{E}_L \mid)f] - \frac{f}{\tau(E)} + Q(E), \tag{4}$$

where $D(E)$ and $A(E)$ are the diffusion and systematic acceleration coefficients, $\dot{E}_L$ represents the energy losses, $\tau(E)$ is the trapping time and $Q(E)$ is the source function. A steady-state solution is often sought ($\partial f/\partial t \approx 0$). This process was studied in the context of hard X-ray looptop sources by Petrosian and Donaghy (1999), who used parametric models for the plasma turbulence, though with parameters consistent with the more detailed calculations of Pryadko and Petrosian (1997), to investigate the dependence of looptop to footpoint intensity and spectral ratios as a function of acceleration, scattering and escape times. These authors derived simplified expressions for the ratio of looptop to footpoint intensities at a given photon energy, finding that in the case of an isotropic electron distribution and a relatively steep spectrum it depends primarily on the ratio of the Coulomb scattering timescale to the trap escape timescale at that energy. Observed *Yohkoh* HXT looptop flare properties could be reproduced by the models, using reasonable densities (a few $\times\ 10^{10}$ cm^{-3}), magnetic fields (a few $\times 100$ G) and acceleration and escape timescales (a few $\times 10^2$ s) but the discriminating power of the observations was poor, and a comprehensive analysis using RHESSI data has not yet appeared (but see Liu et al. 2008).

3.3.4 Soft-hard-soft spectral behavior

The soft-hard-soft pattern dominates the hard X-ray spectral evolution in the impulsive phase (Sect. 2.2). Simultaneously appearing coronal hard X-ray sources in the impulsive phase often appear to share this property (Sect. 2.4.3)—though other types of coronal hard X-ray sources often show progressive spectral hardening instead. The "soft-hard-soft" (SHS) evolution of the impulsive phase spectrum (see Sect. 2.2)

is thus an important constraint for acceleration models. In this context, Grigis and Benz (2006) studied the transit-time model of turbulent acceleration, concluding that although the turbulent magnetic trap can reproduce the observed SHS characteristics (Benz 1977; Brown and Loran 1985) it fails to reproduce other details, for example the energy of ≈20 keV at which the "pivot point" appears (Gan 1998; Grigis and Benz 2006).

3.3.5 Origins of coronal turbulence

The discussion above assumes ad hoc a level of turbulence with specified characteristics. A number of different flare processes have been proposed as turbulence sources. Miller et al. (1996) suggest that small-amplitude fast-mode waves formed at a large scale by magnetic reconnection cascade to smaller wavelengths, on a timescale approximately equal to the signal-crossing timescale for the largest fluctuation (i.e. the Alfvén crossing timescale or the eddy turnover timescale, for strongly/weakly magnetized situations). Larosa and Moore (1993) propose that the turbulence develops in a sheared reconnection outflow. However, the overall picture of the rapid development of a turbulent cascade is not certain. The manner of development of an MHD turbulent cascade is the subject of a vast literature, but the bottom line is that in MHD turbulence, collisions between oppositely directed wavepackets are necessary; see e.g. the discussion in Goldreich and Sridhar (1997), and the requirement to do work against the permeating magnetic field inhibits the production of a parallel cascade. The cascade timescale may well be the longest timescale in the system (particularly if a cascade to a state of isotropic turbulence is sought) and this therefore limits the volumetric energy gain rate of the electrons.

One can also find a physical basis for coronal turbulence in the many developments of the Parker problem (Parker 1983): i.e. the response of the coronal magnetic field to driving by footpoint motion. It has been shown by e.g. van Ballegooijen (1986) and Turkmani et al. (2005) that footpoint stressing—both random and systematic—leads to the development of a hierarchy of scales of magnetic disturbances. Current-sheet formation over this range of scales leads to dissipation of magnetic energy in discrete events, usually following a power-law distribution. While normally associated with coronal heating, such a scenario might also lead to large events (flares); see Fig. 14a (Turkmani et al. 2005, 2006; Onofri et al. 2006).

This example of a resistive MHD simulation (Fig. 14) shows the presence of a highly structured electric field in the corona. Test particles can then be tracked in these fields. The blue and red regions in the left panel of Fig. 14 show electric fields pointing to the opposite footpoints (the left and right faces of the volume), and the distribution function of the electric field strength is shown in the right panel of Fig. 14. The fields are much stronger than the Dreicer field, and when the particle crosses a specific current sheet it may lose or gain energy. Such stochastic electric fields can then confine particles at the top of the loop and accelerate them at the same time. Turkmani et al. (2006) examine loops with density $n \approx 10^9$ cm^{-3} and find collisions to be important only at the footpoints. Enhancing the density inside the loop can produce looptop hard X-rays, as can greater field complexity (Gkioulidou et al. 2007). Similar results demonstrating the efficiency of particle acceleration in fully developed MHD

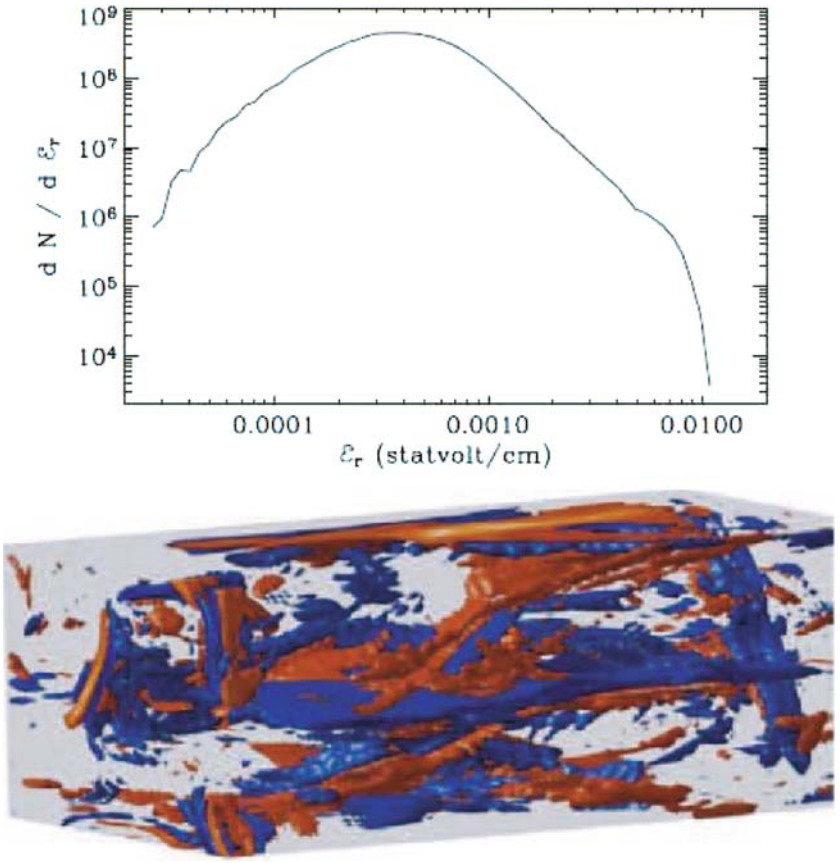

Fig. 14 *Left* snapshot of the resistive electric field configuration inside a coronal loop driven by random motions of the magnetic footpoints at the left and right faces of the simulation box; and *top* the distribution function of electric field strength seen by a typical particle traveling inside this "loop." The *red* and *blue* indicate fields pointing towards opposite faces of the box. From Turkmani et al. (2006)

turbulence were presented by Dmitruk et al. (2004): see also Larosa et al. (1996) for another scenario involving strong turbulence.

The above simulations rely on resistive electric fields, but explicitly do not incorporate the microphysics of magnetic reconnection in the current sheets which is likely to involve electron inertia, anomalous resistivity, anisotropic pressure tensors, or indeed all three. An example of this alternative approach can be found in Drake et al. (2005) via a 3D particle code; this work demonstrated the formation of numerous magnetic filaments inside the current sheet that act as Fermi accelerators (see Fig. 15). This development suggests the possibility of putting the results from models of turbulent loops on a more self-consistent physical footing.

Making the connection between the above work, and the (often quasi-linear) "equation-oriented" approach discussed in Sect. 3.3.3 and in numerical approaches (e.g., Miller et al. 1996) is more difficult. It should be stressed that both approaches

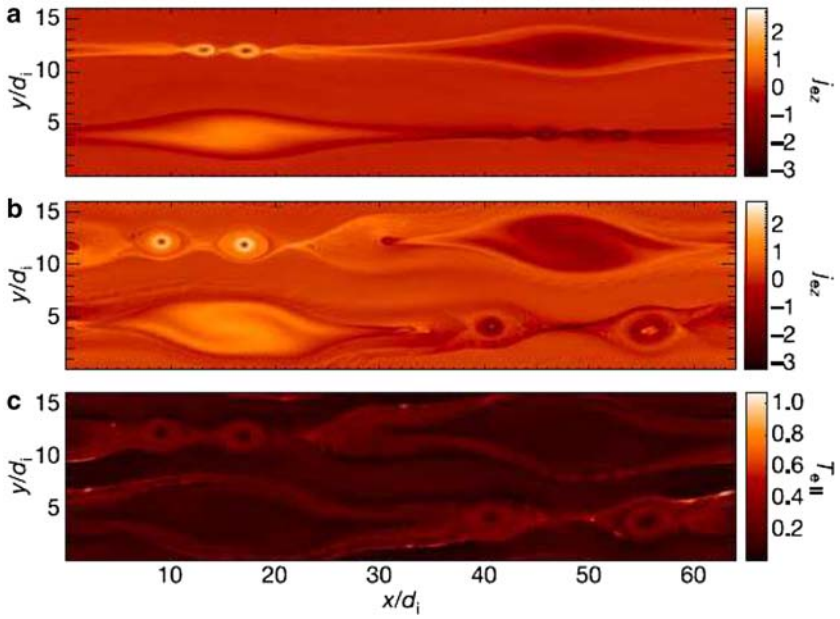

Fig. 15 Particle-in-cell simulations of island evolution during reconnection (Drake et al. 2006). **a**, **b** Out-of-plane current densities at two times, and **c** the mean electron energy at the latter time

have advantages. The former treats a far larger range of scales, and permits tracking the distribution function; the latter includes a consistent driver, and does not make assumptions such as the quasi-linear approximation. However, while both theories are still incomplete, the generic "stochastic" or "turbulent" acceleration models for coronal hard X-ray sources, can in principle account for the formation of loop-top sources and the footpoint spectral evolution (the soft-hard-soft pattern). Recent numerical work in the resistive MHD or Hall MHD approximations (Dmitruk et al. 2004; Turkmani et al. 2005, 2006; Gkioulidou et al. 2007) points the way to more complete numerical models of the acceleration. Future models must also treat the feedback of the particle distributions on the accelerator—the MHD turbulence and current sheets.

3.4 Large-scale shock waves

Particle acceleration by large-scale shock waves, though theoretically difficult, has overwhelming observational support as an explanation for solar energetic particles in the heliosphere (e.g., Reames 1999), especially for energetic ions but also for the low-energy electrons observed around the shock passage near one AU. While in the past decade ion acceleration at shocks, and particularly the so-called "injection problem" (e.g., Ellison et al. 1996), have become well understood, electron acceleration remains problematic. So-called shock drift acceleration can produce a small flux of moderate energy electrons at a quasi-perpendicular shock. Diffusive (Fermi) acceleration of electrons is believed to occur above a certain electron energy needed to permit

scattering, but at this time the "injection problem" (the ability to accelerate particles in the thermal pool up to the critical energy where shock acceleration can take over) is unsolved for electrons.

We know empirically from the radio signatures of type II bursts, for example, that coronal shocks can accelerate non-thermal electrons to low energies (e.g. Wild et al. 1963), and this process can be observed operating in the heliosphere (Bale et al. 1999) as well. Under appropriate conditions high-energy electrons may also be accelerated in this way (Holman and Pesses 1983; Mann et al. 2001), and shock-accelerated high-energy electrons have been observed (e.g., Simnett 2003). The problem lies in understanding the geometry of shock excitation and propagation with respect to the observed coronal hard X-ray sources. For a large-scale loop with a long-lasting population of high-energy electrons, we would want the shock to form *below* the structure to be effective, and at the same time not to disrupt it as a CME expands. Large-scale shock waves in association with CMEs are known from their Moreton-wave and radio signatures (e.g., Pick et al. 2006) to propagate in the corona at heights below about 0.5 $R_\odot$ However, we note that the moving coronal hard X-ray sources (Sect. 2.2.6) have speeds that tend to associate them with the body of a CME, rather than its emission front or any bow shock.

3.5 Super-hot thermal coronal sources

Coronal hard X-rays that can be explained as thermal sources (see Sect. 2.3.1) require temperatures on the order of 30 MK and above (Lin et al. 1981), and almost certainly involve the relaxation of distribution functions from distributions originally having non-thermal tails. Such sources occur at all different times in the flare, and the larger-scale coronal sources, with reduced collisionality, may provide good observational information about how a plasma thermalizes.

A significant body of work has developed to model the process termed "chromospheric evaporation," usually proposed as the means by which coronal loops are filled with hot plasma. The most recent and most elaborate single-loop radiation hydrodynamic modelling, by Allred et al. (2005), includes electron beam energy deposition, hydrodynamics, classical conduction, and radiative losses in both optically thin and optically thick radiations. Multiple single-loop models have also been combined to reproduce the emission observed in realistic flares, where we know that multiple loops, "lighting up" at different times, are involved (Hori et al. 1998; Aschwanden and Alexander 2001; Warren 2006). A basic result of all of such models as they currently stand is that, while the required coronal density increase can be obtained for mostly reasonable energy fluxes per unit area into the chromosphere, the temperature increase cannot. For example, in the Allred et al. (2005) simulations, a value of 10^{11} erg $(\mathrm{cm}^2\ \mathrm{s})^{-1}$—equivalent to a very large flare—cannot increase the coronal temperature beyond 10 MK, which is still much too cool to be relevant to the observations.

To obtain temperatures consistent with the Masuda source for example, Warren (2006) requires up to 10^{13} erg $(\mathrm{cm}^2\ \mathrm{s})^{-1}$; this is many times the photospheric radiant energy flux. An electron beam with this energy flux cannot—according to our current understanding—propagate stably through a corona with reasonable physical parame-

ters. To explain thermal hard X-ray coronal sources by evaporation may still require coronal energy input by something other than an electron beam; in a plasma one generally must consider the physics of the return current for the beam (e.g. van den Oord 1990). There is little literature yet on the consequences of this physics for the coronal hard X-ray sources.

3.6 Summary of theory

The observed coronal hard X-ray sources pose the usual major questions: how are the electrons accelerated, how can they be trapped in the corona for minutes or hours; and how are they related to the fundamental problems of flare physics. The distinction from previous work on flare hard X-rays is that we are now able to observe sources that systematically differ from the standard paradigm of the impulsive phase: the thick-target model with hard X-ray footpoints, soft-hard-soft spectral behavior, and the Neupert effect. The coronal hard X-ray sources may exhibit none of these features or else display them in clearly different ways.

Of the models discussed, the most attractive appear to be those involving turbulent acceleration/trapping in the corona, and acceleration in a collapsing trap. However, in the turbulent model the relation of the acceleration physics to the overall magnetic geometry and evolution is unspecified and unclear, the treatment of turbulence is ad hoc, and the link to reconnection microphysics (in the case of turbulent current sheets) not yet made due to the great range of scales in the problem. The collapsing trap model for its part is attractive due to its ability to link the acceleration to large-scale changes in the coronal magnetic field, but it is not clear that it can provide the required energies. Indeed, we do not know the details of the magnetic geometry, especially during the rapid restructuring necessary to release flare energy or launch a CME. Thus the RHESSI imaging spectroscopy in a sense is providing more information than theories can yet handle.

4 Conclusions and future developments

The material presented above makes it clear that we can detect hard X-ray emission from all phases of solar flares. The observations reflect non-thermal emissions from electrons over a wide range of energies (few keV for the double coronal type, to MeV for the coronal γ-ray sources) as well. Table 1 summarizes the observations by class of event. In most cases we do not have enough observations to support a proper classification into observationally distinct categories. We see clear hints that the coronal hard X-ray sources may have different physics (for example, acceleration mechanisms) in some cases. The normal paradigm for solar hard X-ray consists of the impulsive-phase footpoint brightening, the Neupert effect, and the soft-hard-soft spectral evolution. Because some of our coronal hard X-ray sources may differ, we feel that they are well worth study and may provide interesting new ideas for non-solar applications.

In the meanwhile we have shown how sketchy our solar observations really are. They are limited by sensitivity (the sources may be bright, but they are also highly

time-variable) and by image dynamic range. The root cause of this latter problem is the brightness of the footpoint sources in most cases; the most interesting coronal sources tend to occur in conjunction with the very brightest impulsive-phase hard X-ray sources, and in the later phase of a flare, in competition with extremely intense thermal emission from coronal loops. The RHESSI attenuator system and its two-segment detector design (Lin et al. 2002) have helped enormously with these observational problems, but much more remains to be done. We suggest that focusing optics at grazing incidence may help to suppress image background levels and thus make it possible to observe faint coronal sources such as the electron streams known to produce radio type III bursts (e.g., Krucker et al. 2008) in the near vicinity of a flare. This capability should be accompanied by larger effective area. Solar flare observations traditionally emphasize the brightest sources (they tend to have the most comprehensive data coverage), rather than the faintest (the brighter objects tend to have already been studied) as in nightttime astronomy, so there are great ranges of yet-unexplored parameter space. In other words, the solar corona is quite bright in absolute terms.

Solar hard X-ray observations have not yet achieved sufficient sensitivity for us to study energy–release phenomena that have been well-known for many decades from metric-band radio observations, but have never been susceptible to observations at shorter wavelengths. The type III burst electrons are one example, but equally we should be able to observe particle acceleration in shock fronts associated with eruptive flares and CMEs (Kahler and Ragot 2008). The powerful non-thermal phenomena that occur in the corona following the most powerful flare/CME processes remain mysterious, and better data are needed to understand how particle acceleration can occur so late in such events, well after the dominant energy release in the impulsive phase.

Acknowledgments The authors thank the International Space Science Institute, Bern, for supporting the preparation of this paper. A. Caspi and P. St.-Hilaire provided valuable help, and J. Drake commented thoughtfully on an early version of the manuscript. The authors thank NASA (grant NAS 5-98033) for support for this work through the RHESSI program. L. Fletcher would also like to acknowledge support by the European Commission via the SOLAIRE Network (MTRN-CT-2006-035484). The review material in this paper made extensive use of NASA's Astrophysics Data System (ADS), for which the authors are grateful.

5 Appendix A: Emission mechanisms revisited

Electrons passing through a cosmic gas will interact with other atoms and ions, any bulk magnetic field and the photons of any ambient radiation field. The resulting free-bound (recombination), free-free (bremsstrahlung), synchrotron and inverse Compton mechanisms are well understood (e.g., Blumenthal and Gould 1970; Tucker 1975; Rybicki and Lightman 1979). At the level of quantum electrodynamics, the last three of these are essentially the same process, involving the scattering by electrons of real photons, or the virtual photons mediating electrostatic or magnetic fields. All of these mechanisms can in principle contribute to hard X-ray production but to varying degrees depending on the gross properties of the ambient plasma and the energy distribution of the accelerated electrons. Coherent emission of X-rays via some plasma process

seems implausible, requiring $n_e \approx 10^{29}$ cm^{-3} if it were to occur analogously to Type III radio bursts, for example.

Korchak (1967, 1971) considered the relative contributions of the bremsstrahlung, inverse Compton and synchrotron mechanisms for plausible flare electron energies in the solar atmosphere. He concluded that bremsstrahlung would normally dominate hard X-ray production and that an inverse Compton contribution might sometimes be significant, particularly in the low ambient density conditions relevant here. A significant synchrotron contribution was found highly unlikely. He did not consider recombination radiation.

Here we revisit Korchak's discussion, giving a few useful results for the photon spectra produced by the various mechanisms, and comment briefly on relevance to coronal hard X-ray sources.

5.1 Synchrotron radiation

Non- to mildly-relativistic electrons radiate at the gyrofrequency

$$\nu_B = 2.8 \times 10^6 B$$

(in Hz, with magnetic field strength B in G) and its first few harmonics. Even for sunspot magnetic fields in the kG range, this cyclotron radiation lies in the radio part of the spectrum.

If electrons are relativistic with speed βc, the gyrofrequency is shifted by a factor $\gamma = \left(1 - \beta^2\right)^{-1/2}$, harmonics merge to form a continuum and radiation is found in the wavelength range given by the *synchrotron frequency* (Blumenthal and Gould 1970; Ginzburg and Syrovatskii 1969), equivalent to a photon energy of

$$\epsilon_S = 1.74 \times 10^{-11} \gamma^2 B \,\text{keV}.$$

Likely coronal fields in the 100–1,000 G range then necessitate electron energies of 10s of GeV. We know that positrons of 100s of MeV are certainly produced in some flares via $p - p$ collisions and pion decay (Murphy et al. 1987); and electrons of 10s of MeV energies are observed in the interplanetary medium (Moses et al. 1989). These are the highest known energies attained by electrons in flares, however. There is no evidence at all for electrons of the energies needed for a significant synchrotron contribution to hard X-ray's and we do not consider this possibility further.

5.2 Inverse Compton radiation

Consider an electron of energy $\gamma m_e c^2$ encountering a photon of energy ϵ_i. After the encounter the photon has an energy ϵ' which depends in detail on the kinematics of the collision but has a maximum value of $4\gamma^2 \epsilon_i$. To within a factor of order unity

$$\epsilon' \approx eq\, \gamma^2 \epsilon_i$$

(e.g., Tucker 1975; Blumenthal and Gould 1970) for most encounters, in the limit $\gamma \gg 1$. Thus, to scatter photospheric photons of typical energy 2 eV into the hard X-ray range (say, 20 keV) we need electrons with energies in the region of 50 MeV. Such electrons (or positrons) are certainly present in some large, energetic flares at least (e.g., Moses et al. 1989; Vilmer et al. 2003; Rieger et al. 1983). To scatter 1 keV soft X-ray photons to 100 keV needs only 5 MeV electrons, for which there is hard X-ray and radio evidence in many flares. Such photons are many orders of magnitude less numerous than optical, photospheric photons, however.

To correctly calculate the inverse Compton photon spectrum we need to integrate over both the electron and photon velocity distributions, paying proper attention to kinematics and weighting by the appropriate (Thomson or Klein-Nishina) cross-section. Explicit results have been obtained in the relativistic limit for some special cases. We quote one of these here, simple enough to be useful for first estimates. It gives the volume emissivity j_ϵ (photons keV^{-1} s^{-1}) produced by isotropic, relativistic electrons ($\gamma \gg 1$) interacting with isotropic, mono-energetic photons of energy ϵ_i:

$$I_{IC}(\epsilon) = \frac{8\pi r_0^2 c}{\epsilon} n_\nu N_0 (\delta - 1) \left(\frac{E_0}{mc^2}\right)^{\delta-1} Q(\delta) \left(\frac{\epsilon}{4\epsilon_i}\right)^{(1-\delta)/2} \quad (5)$$

(Blumenthal and Gould 1970; Tucker 1975). Here n_ν is the photon number density (cm^{-3}), N_0 is the local fast electron density or the total number of electrons in a homogeneous source above energy E_0, r_0 is the classical electron radius and electrons have been assumed to have a kinetic energy distribution function $\approx E^{-\delta}$. The (order unity) function Q is given by

$$Q(\delta) = \frac{2\left(11 + 4\delta + \delta^2\right)}{(1+\delta)(3+\delta)^2(5+\delta)}.$$

The photon density n_ν is a crucial parameter here. Attributing all of the solar luminosity of 4×10^{33} erg s^{-1} to 2 eV photons gives $n_\nu \approx 10^{12}$ cm^{-3}.

The solar spectrum is of course not composed of mono-energetic photons of 2 eV. Analytical expressions for more elaborate photon distribution functions have been obtained, e.g. for the inverse Compton spectrum resulting from a blackbody photon distribution (Blumenthal and Gould 1970; Tucker 1975). Equation (5) is more restricted in applicability, but more immediately informative for order-of-magnitude purposes. Note that it does assume that the electron power-law energy distribution extends to arbitrarily high energies. If there is a maximum electron energy $\gamma_{\max} mc^2$, the inverse Compton photon spectrum will steepen and tail off to zero at $\epsilon_{\max} = 4\gamma_{\max}^2 \epsilon_i$.

Inverse Compton radiation from highly relativistic electrons is beamed, with a cone of emission of angular width $\approx \gamma^{-1}$. If emitting electrons are not isotropic, as assumed in (5), the intensity of the radiation may depend strongly on viewing angle. Electrons travelling e.g. along the field lines in a loop magnetic structure could produce apparent isolated patches from the point of view of a particular observer.

5.3 Bremsstrahlung versus inverse Compton

Ever since Korchak's work, flare hard X-rays have been interpreted as electron-ion bremsstrahlung. An electron–electron component becomes significant for $\epsilon \gtrsim 300$ keV (Haug 1975; Kontar et al. 2007). Restricting attention to lower energies than this, the bremsstrahlung emissivity $j(\epsilon)$ (keV^{-1}s^{-1}) of a population $n(E)$ (keV^{-1}cm^{-3}) of electrons in a fully ionized hydrogen medium of density n_p (cm^{-3}) is given by

$$j_{\rm BR}(\epsilon) \;=\; n_p V \int_{\epsilon}^{\infty} N(E) v(E) \frac{{\rm d}\sigma}{{\rm d}\epsilon}(\epsilon, E)\, {\rm d}E \tag{6}$$

We have neglected the directionality of bremsstrahlung in the 10 s of keV energy range so there is no dependence on viewing angle and electron angular distribution. In contrast to inverse Compton or synchrotron radiation, bremsstrahlung photons of energy ϵ are produced by electrons with energies $E \geq \epsilon$. Equation (6) is, again, averaged over viewing angle or, equivalently, appropriate to an isotropic distribution. At relativistic energies electron-electron bremsstrahlung becomes comparable to the electron-ion component (see Sect. 2.3.3 for relevant observations).

Expressions for the bremsstrahlung cross-section ${\rm d}\sigma/{\rm d}\epsilon$ have been found in various limits (non-relativistic, ultra-relativistic, etc.); see Koch and Motz (1959). The simplest possible (Kramers) approximation is useful for first estimates in the non-relativistic regime:

$$\epsilon \frac{{\rm d}\sigma}{{\rm d}\epsilon} \;=\; \frac{4\sqrt{2}}{3} \alpha r_0^2 \frac{m_{\rm e} c^2}{E},$$

where α is the fine-structure constant. Inserting this cross-section in (6) and adopting the same power-law energy distribution as above, we find

$$j_{\rm BR}(\epsilon) \;=\; \frac{8}{3} \frac{\alpha r_0^2 c}{\epsilon} \frac{2(\delta-1)}{(2\delta-1)} n_p N_0 \left(\frac{E_0}{m_{\rm e} c^2}\right)^{\delta-1} \left(\frac{\epsilon}{m_{\rm e} c^2}\right)^{1/2-\delta}. \tag{7}$$

Similar expressions may be found for more elaborate cross-sections e.g. in Brown (1976).

We can rewrite (7) usefully as follows. Suppose we view an isolated hard X-ray source of angular size α at distance D so that its volume is $\approx (\alpha D)^3$. Let electrons of energies $\geq E_0$ constitute a fraction η of all electrons in the source volume. Then the observed photon flux from the whole source at $D = 1$ AU is $j(\epsilon) = A\epsilon^{-\delta-1/2}$ where

$$A \;=\; 0.01 \eta n_9^2 \alpha^3 \frac{2(\delta-1)}{2\delta-1} E_0^{\delta-1}$$

and α is now measured in arcsec and n_9 is density in units of 10^9 cm$^-$3.

Observing at photon energy $\epsilon \ll m_e c^2$, suppose we view a region in which electrons have an energy distribution $N(\epsilon) \approx E^{-\delta}$ extending to arbitrarily high energies. The relative magnitudes of inverse Compton and bremsstrahlung contributions obey

$$\frac{j_{IC}(\epsilon)}{j_{BR}(\epsilon)} = \frac{3}{2\alpha}\frac{n_v}{n_p}(2\delta - 1)Q(\delta)\left(\frac{\epsilon}{4\epsilon_i}\right)^{(1-\delta)/2}\left(\frac{\epsilon}{m_e c^2}\right)^{\delta-1/2}.$$

Inverse Compton radiation, with its harder photon spectrum, eventually dominates over bremsstrahlung. With an ambient coronal density of 10^9 cm^{-3}, $n_v/n_p = 1{,}000$ and this ratio may approach or exceed unity, in the 10–100 keV photon energy range, for the hardest likely energy distributions (e.g. $\delta = 2$). If there are regions where the ambient density appears to be too low for consistency with observed hard X-rays, an inverse Compton contribution should perhaps be considered.

This brief discussion assumes that electrons are present with $E \approx \epsilon$. If most electrons had energies $\gg \epsilon$, the bremsstrahlung contribution at ϵ would be depressed compared to the estimates above. Any anisotropy of photon and electron distributions will also revise the spectrum from the form (5), in a way dependent on the details of these distributions referred to viewing angle.

5.4 Recombination radiation

Considered unimportant for decades (since Culhane and Acton 1970), recombination radiation has recently received renewed attention. The higher iron abundance now believed appropriate to the solar atmosphere is a key factor in this revision (Brown, private communication). Brown and Mallik (2008) suggest that it may contribute significantly to flare X-rays in the 10–40 keV range, particularly if the emitting electrons recombine in a region of high ambient temperature (>10^7 K, so that most species are ionized) and have a steeply falling energy distribution (e.g. $\delta = 5$). The requirement for a hot plasma makes a recombination contribution particularly likely from coronal hard X-ray sources. The sharp emission edges in the recombination continuum could in principle map out features in the electron spectrum, and so there is in principle important diagnostic potential in observing it (Brown and Mallik 2008). At present there is no observational evidence for this process in the hard X-ray continuum, unfortunately.

5.5 Thick targets

The phrase “thick target” was introduced in laboratory studies of hard X-ray production to refer to a situation in which bombarding particles encounter a target thick enough to stop them completely (e.g., Koch and Motz 1959). It is vital to distinguish between the energy distribution injected into such a source and the mean energy distribution representative of the source as the emitting electrons slow down. All the results above are for electron distributions frozen at one instant. The relative importance of bremsstrahlung and inverse Compton radiation, for instance, will change as electrons evolve in energy, but qualitative conclusions from the above are unchanged.

Expressions for hard X-ray spectra from solar thick-target situations were first given in Brown (1971). These are not obviously appropriate, without further consideration, to coronal sources unless electrons actually stop within the region being studied.

6 Appendix B: Coronal time scales

Assuming a simple slowly varying coronal magnetic field, charged particles will follow the adiabatic motions allowed to them by the large-scale geometry. In the absence of wave-particle interactions, this means that particles will gyrate around the field in the Larmor motion, bounce back and forth along it between mirror points, and execute drift motions. The solar magnetic field on active-region scales does not have axisymmetry with respect to the body of the Sun, so these drifts eventually result in particle loss. In the meanwhile, in the absence of wave-particle interactions, energetic electrons may be trapped while they lose energy to collisional and synchrotron losses.

Figure 16 shows representative time scales for electron collisional losses, synchrotron losses, and adiabatic drift motions. These assume 90° pitch angles and therefore represent upper limits for particles that can generally penetrate to lower-lying mirror points. The defaults for these curves are (n_e, B, $\ell = B/\nabla B$) = (10^8 cm^{-3}, 10 G, and 7×10^9 cm), respectively. The total radiated power in the synchrotron emission spectrum is given by

$$P = 1.59 \times 10^{-7} B^2 \gamma^2 \beta^2 \text{erg/s}$$

for relativistic γ and β; the synchrotron time scale thus scales as $(\gamma B)^{-2}$ and so it could compete with the dominant Coulomb collisions for large pitch angles at the higher energies. The collision loss time scales as $(n_e \beta)^{-1}$ and the drift time as $\ell^2 \beta^{-2} B$, where n_e is the density and ℓ a scale length for the magnetic field strength.

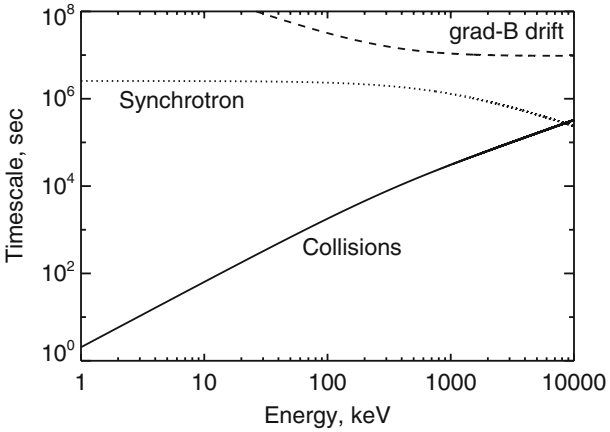

Fig. 16 Representative time scales for fast electrons in the solar corona: *solid* the Coulomb collision time assuming a density of 10^8 cm^{-3}, *dotted* synchrotron radiation assuming B = 10 G, *dashed* gradient-B drift over a spatial scale of 0.1 $R_\odot$

From Fig. 16 we see that collisional losses dominate synchrotron losses at lower energies. In the absence of wave–particle interactions, this implies a long trapping time for electrons in a mirror geometry, which should generally prevail in a coronal magnetic field with weak currents. Hard X-ray production scales with the collisional energy losses, so in a thick-target sense—integrating over the lifetime of the electrons—the ratio of synchrotron emission to bremsstrahlung emission will increase in proportion to the trapping time.

References

Alexander D, Katsev S (1996) Geometrical considerations in imaging the solar corona. Solar Phys 167:153–166

Alexander D, Metcalf TR (1997) A spectral analysis of the masuda flare using *Yohkoh* Hard X-ray telescope pixon reconstruction. ApJ 489:442, doi:10.1086/304762

Alfvén H, Carlqvist P (1967) Currents in the solar atmosphere and a theory of solar flares. Solar Phys 1:220–228, doi:10.1007/BF00150857

Allred JC, Hawley SL, Abbett WP, Carlsson M (2005) Radiative hydrodynamic models of the optical and ultraviolet emission from solar flares. ApJ 630:573–586, doi:10.1086/431751, arXiv:astro-ph/0507335

Antiochos SK, Sturrock PA (1978) Evaporative cooling of flare plasma. ApJ 220:1137–1143, doi:10.1086/155999

Asai A, Nakajima H, Shimojo M, White SM, Hudson HS, Lin RP (2006) Preflare nonthermal emission observed in microwaves and Hard X-rays. PASJ 58:L1–L5

Aschwanden MJ (2002) Particle acceleration and kinematics in solar flares. A synthesis of recent observations and theoretical concepts (Invited Review). Space Sci Rev 101:1–227, doi:10.1023/A:1019712124366

Aschwanden MJ, Alexander D (2001) Flare plasma cooling from 30 MK down to 1 MK modeled from *Yohkoh*, GOES, and TRACE observations during the Bastille Day Event (14 July 2000). Solar Phys 204:91–120, doi:10.1023/A:1014257826116

Aschwanden MJ, Wills MJ, Hudson HS, Kosugi T, Schwartz RA (1996) Electron time-of-flight distances and flare loop geometries compared from CGRO and *Yohkoh* observations. ApJ 468:398, doi:10.1086/177700

Aschwanden MJ, Fletcher L, Sakao T, Kosugi T, Hudson H (1999) Deconvolution of directly precipitating and trap-precipitating electrons in solar flare Hard X-rays. III. *Yohkoh* Hard X-ray telescope data analysis. ApJ 517:977–989

Bai T (1982) Transport of energetic electrons in a fully ionized hydrogen plasma. ApJ 259:341–349, doi:10.1086/160170

Bai T, Ramaty R (1979) Hard X-ray time profiles and acceleration processes in large solar flares. ApJ 227:1072–1081

Bale SD, Reiner MJ, Bougeret JL, Kaiser ML, Krucker S, Larson DE, Lin RP (1999) The source region of an interplanetary type II radio burst. GRL 26:1573–1576, doi:10.1029/1999GL900293

Bastian TS, Benz AO, Gary DE (1998) Radio emission from solar flares. ARAA 36:131–188, doi:10.1146/annurev.astro.36.1.131

Battaglia M, Benz AO (2006) Relations between concurrent hard X-ray sources in solar flares. A&A 456:751–760, doi:10.1051/0004-6361:20065233, arXiv:astro-ph/0606353

Battaglia M, Benz AO (2007) Exploring the connection between coronal and footpoint sources in a thin-thick target solar flare model. A&A 466:713–716, doi:10.1051/0004-6361:20077144, arXiv:astro-ph/0702309

Benz AO (1977) Spectral features in solar hard X-ray and radio events and particle acceleration. ApJ 211:270–280

Bespalov PA, Zaitsev VV, Stepanov AV (1987) On the origin of time delays in hard X-ray and gamma-ray emission of solar flares. Solar Phys 114:127–140

Blackman EG, Field GB (1994) Nonthermal acceleration from reconnection shocks. Phys Rev Lett 73:3097–3100, arXiv:astro-ph/9410036

Blumenthal GR, Gould RJ (1970) Bremsstrahlung, synchrotron radiation and Compton scattering of high-energy electrons traversing dilute gases. Rev Mod Phys 42:237–270

Bogachev SA, Somov BV (2007) Formation of power-law electron spectra in collapsing magnetic traps. Astron Lett 33:54–62, doi:10.1134/S1063773707010070
Bohlin JD, Frost KJ, Burr PT, Guha AK, Withbroe GL (1980) Solar maximum mission. Solar Phys 65:5–14, doi:10.1007/BF00151380
Bone L, Brown JC, Fletcher L, Veronig A, White S (2007) Birth and evolution of a dense coronal loop in a complex flare region. A&A 446:339–346, doi:10.1051/0004-6361:20020947
Brown JC (1971) The deduction of energy spectra of non-thermal electrons in flares from the observed dynamic spectra of Hard X-Ray bursts. Solar Phys 18:489
Brown JC (1973) The temperature structure of chromospheric flares heated by non-thermal electrons. Solar Phys 31:143
Brown JC (1976) The interpretation of hard and soft X-rays from solar flares. R Soc Lond Philos Trans Ser A 281
Brown JC, Hoyng P (1975) Betatron acceleration in a large solar hard X-ray burst. ApJ 200:734–746
Brown JC, Loran JM (1985) Possible evidence for stochastic acceleration of electrons in solar hard X-ray bursts observed by SMM. MNRAS 212:245–255
Brown JC, Mallik PCV (2008) Non-thermal recombination—a neglected source of flare hard X-rays and fast electron diagnostic. A&A 481:507–518
Brown JC, Melrose DB (1977) Collective plasma effects and the electron number problem in solar hard X-ray bursts. Solar Phys 52:117–131
Brown JC, Carlaw VA, Cromwell D, Kane SR (1983) A comparison of the thick-target model with stereo data on the height structure of solar hard X-ray bursts. Solar Phys 88:281–295
Brown JC, Aschwanden MJ, Kontar EP (2002) Chromospheric height and density measurements in a solar flare observed with RHESSI I. Theory. Solar Phys 210:373–381, doi:10.1023/A:1022469402781
Brueckner GE, Howard RA, Koomen MJ, Korendyke CM, Michels DJ, Moses JD, Socker DG, Dere KP, Lamy PL, Llebaria A, Bout MV, Schwenn R, Simnett GM, Bedford DK, Eyles CJ (1995) The large angle spectroscopic coronagraph (LASCO). Solar Phys 162:357–402, doi:10.1007/BF00733434
Cargill PJ (2001) Theories of heating and particle acceleration in the solar corona. Adv Space Res 26:1759–1768
Cargill PJ, Priest ER (1983) The heating of postflare loops. ApJ 266:383–389, doi:10.1086/160786
Caspi A, Lin RP (2008) RHESSI X-ray continuum and Fe-to-Fe/Ni line ratio measurements of thermal flare plasma (in preparation)
Cliver EW, Dennis BR, Kiplinger AL, Kane SR, Neidig DF, Sheeley NR, Koomen MJ (1986) Solar gradual hard X-ray bursts and associated phenomena. ApJ 305:920–935
Conway AJ, MacKinnon AL (1998) The electron cyclotron maser in hot thermal plasmas. A&A 339:298–308
Culhane JL, Acton LW (1970) A simplified thermal continuum functionfor the X-ray emission from coronal plasmas. MNRAS 151:141
Dalla S, Browning PK (2005) Particle acceleration at a three-dimensional reconnection site in the solar corona. A&A 436:1103–1111, doi:10.1051/0004-6361:20042589
Dauphin C, Vilmer N (2007) Time delay between γ-ray lines and hard X-ray emissions during the 23 July 2002 solar flare interpreted by a trap plus precipitation model. A&A 468:289–298, doi:10.1051/0004-6361:20066247
Dennis BR, Zarro DM (1993) The Neupert effect—What can it tell us about the impulsive and gradual phases of solar flares? Solar Phys 146:177–190
Dmitruk P, Matthaeus WH, Seenu N (2004) Test particle energization by current sheets and nonuniform fields in magnetohydrodynamic turbulence. ApJ 617:667–679
Domingo V, Fleck B, Poland AI (1995) The SOHO mission: an overview. Solar Phys 162:1–2, doi:10.1007/BF00733425
Drake JF, Shay MA, Thongthai W, Swisdak M (2005) Production of energetic electrons during magnetic reconnection. Phys Rev Lett 94(9):095,001
Drake JF, Swisdak M, Che H, Shay MA (2006) Electron acceleration from contracting magnetic islands during reconnection. Nature 443:553–556, doi:10.1038/nature05116
Dreicer H (1959) Electron and ion runaway in a fully ionized gas. I. Phys Rev 115:238–249, doi:10.1103/PhysRev.115.238
Duijveman A, Hoyng P, Machado ME (1982) X-ray imaging of three flares during the impulsive phase. Solar Phys 81:137–157
Ellison DC, Baring MG, Jones FC (1996) Nonlinear particle acceleration in oblique shocks. ApJ 473:1029–+, doi:10.1086/178213, arXiv:astro-ph/9609182

Emslie AG (1978) The collisional interaction of a beam of charged particles with a hydrogen target of arbitrary ionization level. ApJ 224:241–246
Emslie AG, Kontar EP, Krucker S, Lin RP (2003) RHESSI Hard X-Ray imaging spectroscopy of the large gamma-ray flare of 2002 July 23. ApJL 595:L107–L110, doi:10.1086/378931
Emslie AG, Dennis BR, Holman GD, Hudson HS (2005) Refinements to flare energy estimates: a followup to "Energy partition in two solar flare/CME events". J Geophys Res (Space Physics) 110:11,103–+, doi:10.1029/2005JA011305
Énomé S, Tanaka H (1971) Magnetic fields in the lower corona associated with the expanding limb burst on March 30th 1969 inferred from the microwave high-resolution observations. In: Howard R (ed) Solar magnetic fields, IAU Symposium, vol 43, pp 413–+
Feldman U, Hiei E, Phillips KJH, Brown CM, Lang J (1994) Very impulsive solar flares observed with the *Yohkoh* spacecraft. ApJ 421:843–850, doi:10.1086/173696
Feldman U, Laming JM, Doschek GA, Warren HP, Golub L (1999) On the ability of an extreme-ultraviolet multilayer normal-incidence telescope to provide temperature information for solar plasmas. ApJL 511:L61–L64, doi:10.1086/311835
Fletcher L (1995) On the generation of loop-top impulsive hard X-ray sources. A&A 303:L9+
Fletcher L, Hudson HS (2008) Impulsive phase flare energy transport by large-scale Alfvén waves and the electron acceleration problem. ApJ 675:1645–1655, doi:10.1086/527044, arXiv:0712.3452
Fletcher L, Martens PCH (1998) A model for Hard X-Ray emission from the top of flaring loops. ApJ 505:418–431, doi:10.1086/306137
Fletcher L, Hannah IG, Hudson HS, Metcalf TR (2007) A TRACE white light and RHESSI Hard X-Ray study of flare energetics. ApJ 656:1187–1196, doi:10.1086/510446
Forbes TG, Acton LW (1996) Reconnection and field line shrinkage in solar flares. ApJ 459:330, doi:10.1086/176896
Frost KJ, Dennis BR (1971) Evidence from Hard X-Rays for two-stage particle acceleration in a solar flare. ApJ 165:655
Gallagher PT, Dennis BR, Krucker S, Schwartz RA, Tolbert AK (2002) RHESSI and TRACE observations of the 21 April 2002 x1.5 Flare. Solar Phys 210:341–356, doi:10.1023/A:1022422019779
Gan WQ (1998) An invariable point in the energy spectra of non-thermal electrons of solar flares. APSS 260:515–519
Garcia HA (1994) Temperature and emission measure from GOES soft X-ray measurements. Solar Phys 154:275–308
Ginzburg VL, Syrovatskii SI (1969) Developments in the theory of synchrotron radiation and its reabsorption. ARAA 7:375–420
Giuliani P, Neukirch T, Wood P (2005) Particle motion in collapsing magnetic traps in solar flares. I. Kinematic theory of collapsing magnetic traps. ApJ 635:636–646
Gkioulidou M, Zimbardo G, Pommois P, Veltri P, Vlahos L (2007) High energy particle transport in stochastic magnetic fields in the solar corona. A&A 462:1113–1120
Goff CP, van Driel-Gesztelyi L, Harra LK, Matthews SA, Mandrini CH (2005) A slow coronal mass ejection with rising X-ray source. A&A 434:761–771, doi:10.1051/0004-6361:20042321
Gold T (1962) Magnetic storms. Space Sci Rev 1:100–114, doi:10.1007/BF00174637
Goldreich P, Sridhar S (1997) Magnetohydrodynamic turbulence revisited. ApJ 485:680–+, doi:10.1086/304442, arXiv:astro-ph/9612243
Grigis PC, Benz AO (2004) The spectral evolution of impulsive solar X-ray flares. A&A 426:1093–1101, doi:10.1051/0004-6361:20041367, astro-ph/0407431
Grigis PC, Benz AO (2006) Electron acceleration in solar flares: theory of spectral evolution. A&A 458:641–651, arXiv:astro-ph/0606339
Hamilton RJ, Petrosian V (1992) Stochastic acceleration of electrons. I. Effects of collisions in solar flares. ApJ 398:350–358, doi:10.1086/171860
Handy BN, Acton LW, Kankelborg CC, Wolfson CJ, Akin DJ, Bruner ME, Caravalho R, Catura RC, Chevalier R, Duncan DW, Edwards CG, Feinstein CN, Freeland SL, Friedlaender FM, Hoffmann CH, Hurlburt NE, Jurcevich BK, Katz NL, Kelly GA, Lemen JR, Levay M, Lindgren RW, Mathur DP, Meyer SB, Morrison SJ, Morrison MD, Nightingale RW, Pope TP, Rehse RA, Schrijver CJ, Shine RA, Shing L, Strong KT, Tarbell TD, Title AM, Torgerson DD, Golub L, Bookbinder JA, Caldwell D, Cheimets PN, Davis WN, Deluca EE, McMullen RA, Warren HP, Amato D, Fisher R, Maldonado H, Parkinson C (1999) The transition region and coronal explorer. Solar Phys 187:229–260
Haug E (1975) Bremsstrahlung and pair production in the field of free electrons. Z Naturforsch Teil A 30:1099–1113

Heyvaerts J, Priest ER, Rust DM (1977) An emerging flux model for the solar flare phenomenon. ApJ 216:123–137
Hirayama T (1974) Theoretical model of flares and prominences. I. Evaporating flare model. Solar Phys 34:323–338, doi:10.1007/BF00153671
Holman GD, Pesses ME (1983) Solar type II radio emission and the shock drift acceleration of electrons. ApJ 267:837–843, doi:10.1086/160918
Holman GD, Sui L, Schwartz RA, Emslie AG (2003) Electron bremsstrahlung Hard X-ray spectra, electron distributions, and energetics in the 2002 July 23 solar flare. ApJL 595:L97–L101, doi:10.1086/378488
Hori K, Yokoyama T, Kosugi T, Shibata K (1998) Single and multiple solar flare loops: hydrodynamics and Ca XIX resonance line emission. ApJ 500:492, doi:10.1086/305725
Hoyng P , van Beek HF, Brown JC (1976) High time resolution analysis of solar hard X-ray flares observed on board the ESRO TD-1A satellite. Solar Phys 48:197–254
Hoyng P, Duijveman A, Machado ME, Rust DM, Svestka Z, Boelee A, de Jager C, Frost KT, Lafleur H, Simnett GM, van Beek HF, Woodgate BE (1981) Origin and location of the Hard X-ray emission in a two-ribbon flare. ApJL 246:L155+, doi:10.1086/183574
Hudson HS (1972) Thick-target processes and white-light flares. Solar Phys 24:414
Hudson HS (1978) A purely coronal hard X-ray event. ApJ 224:235–240, doi:10.1086/156370
Hudson HS (2000) Implosions in coronal transients. ApJL 531:L75–L77, doi:10.1086/312516
Hudson HS, Fárník F (2002) Spectral variations of flare hard X-rays. In: Wilson A (ed) ESA SP-506: solar variability: from core to outer frontiers, pp 261–264
Hudson HS, Ohki K (1972) Soft X-ray and microwave observations of hot regions in solar flares. Solar Phys 23:155
Hudson H, Ryan J (1995) High-energy particles in solar flares. ARAA 33:239–282, doi:10.1146/annurev.aa.33.090195.001323
Hudson HS, Lin RP, Stewart RT (1982) Second-stage acceleration in a limb-occulted flare. Solar Phys 75:245–261
Hudson HS, Kosugi T, Nitta NV, Shimojo M (2001) Hard X-radiation from a fast coronal ejection. ApJL 561:L211–L214, doi:10.1086/324760
Hurford GJ, Read RB, Zirin H (1984) A frequency angle interferometer for solar microwave spectroscopy. Solar Phys 94:413–426, doi:10.1007/BF00151327
Hurford GJ, Schmahl EJ, Schwartz RA, Conway AJ, Aschwanden MJ, Csillaghy A, Dennis BR, Johns-Krull C, Krucker S, Lin RP, McTiernan J, Metcalf TR, Sato J, Smith DM (2002) The RHESSI imaging concept. Solar Phys 210:61–86, doi:10.1023/A:1022436213688
Jiang YW, Liu S, Liu W, Petrosian V (2006) Evolution of the loop-top source of solar flares: heating and cooling processes. ApJ 638:1140–1153, doi:10.1086/498863, astro-ph/0508532
Kahler SW (1992) Solar flares and coronal mass ejections. ARAA 30:113–141, doi:10.1146/annurev.aa.30.090192.000553
Kahler SW, Ragot BR (2008) Remote sensing of gamma-ray emission from solar energetic proton interactions with the solar wind. ApJ 675:846–852, doi:10.1086/526416
Kane SR (1983) Spatial structure of high energy photon sources in solar flares. Solar Phys 86:355–365
Kane SR, Anderson KA, Evans WD, Klebesadel RW, Laros J (1979) Observation of an impulsive solar X-ray burst from a coronal source. ApJL 233:L151–L155, doi:10.1086/183095
Kane SR, McTiernan J, Loran J, Fenimore EE, Klebesadel RW, Laros JG (1992) Stereoscopic observations of a solar flare Hard X-ray source in the high corona. ApJ 390:687–702, doi:10.1086/171320
Karlický M, Bárta M (2006) X-Ray loop-top source generated by processes in a flare collapsing trap. ApJ 647:1472–1479, doi:10.1086/505460
Karlický M, Kosugi T (2004) Acceleration and heating processes in a collapsing magnetic trap. A&A 419:1159–1168
Kašparová J, Kontar EP, Brown JC (2007) Hard X-ray spectra and positions of solar flares observed by RHESSI: photospheric albedo, directivity and electron spectra. A&A 466:705–712, doi:10.1051/0004-6361:20066689, arXiv:astro-ph/0701871
Kennel CF (1969) Consequences of a magnetospheric plasma. Rev Geophys Space Phys 7:379–419
Kennel CF, Petschek HE (1966) Limit on stably trapped particle fluxes. JGR 71:1–28
Kiplinger AL (1995) Comparative studies of Hard X-ray spectral evolution in solar flares with high-energy proton events observed at earth. ApJ 453:973, doi:10.1086/176457
Klimchuk JA (2000) Cross-sectional properties of coronal loops. Solar Phys 193:53–75
Koch HW, Motz JW (1959) Bremsstrahlung cross-section formulas and related data. Rev Mod Phys 31:920–956

Kontar EP, Brown JC (2006) Stereoscopic electron spectroscopy of solar Hard X-ray flares with a single spacecraft. ApJL 653:L149–L152, doi:10.1086/510586, arXiv:astro-ph/0611170
Kontar EP, Emslie AG, Massone AM, Piana M, Brown JC, Prato M (2007) Electron–Electron Bremsstrahlung emission and the inference of electron flux spectra in solar flares. ApJ 670:857–861, doi:10.1086/521977, arXiv:0707.4225
Kopp RA, Pneuman GW (1976) Magnetic reconnection in the corona and the loop prominence phenomenon. Solar Phys 50:85–98
Korchak AA (1967) Possible mechanisms for generating hard X-rays in solar flares. Sov Astr AJ 11: 258–263
Korchak AA (1971) On the origin of solar flare X-rays. Solar Phys 18:284–304
Kosugi T, Masuda S, Makishima K, Inda M, Murakami T, Dotani T, Ogawara Y, Sakao T, Kai K, Nakajima H (1991) The hard X-ray telescope (HXT) for the Solar-A mission. Solar Phys 136:17–36
Kosugi T, Sakao T, Masuda S, Makishima K, Inda M, Murakami T, Ogawara Y, Yaji K, Matsushita K (1992) The Hard X-ray Telescope (HXT) onboard *Yohkoh*—its performance and some initial results. PASJ 44:L45–L49
Kosugi T, Sakao T, Masuda S, Hara H, Shimizu T, Hudson HS (1994) Hard and Soft X-ray observations of a super-hot thermal flare of 6 February 1992. In: Proceedings of Kofu symposium, pp 127–129
Krucker S, Lin RP (2008) Hard X-ray emissions from partially occulted solar flares. ApJ 673:1181–1187, doi:10.1086/524010
Krucker S, Hannah IG, Lin RP (2007a) RHESSI and Hinode X-ray observations of a partially occulted solar flare. ApJL 671:L193–L196, doi:10.1086/525019
Krucker S, White SM, Lin RP (2007b) Solar flare hard X-ray emission from the high corona. ApJL 669:L49–L52, doi:10.1086/523759
Krucker S, Hurford GJ, MacKinnon AL, Shih AY, Lin RP (2008) Coronal γ-ray Bremsstrahlung from solar flare-accelerated electrons. ApJL 678:L63–L66, doi:10.1086/588381
Kundu MR (1965) Solar radio astronomy. Interscience Publication, New York
Larosa TN, Moore RL (1993) A mechanism for bulk energization in the impulsive phase of solar flares: MHD turbulent cascade. ApJ 418:912, doi:10.1086/173448
Larosa TN, Moore RL, Miller JA, Shore SN (1996) New promise for electron bulk energization in solar flares: preferential fermi acceleration of electrons over protons in reconnection-driven magnetohydrodynamic turbulence. ApJ 467:454, doi:10.1086/177619
Leach J, Petrosian V (1981) Impulsive phase of solar flares. I. Characteristics of high energy electrons. ApJ 251:781–791, doi:10.1086/159521
Leach J, Petrosian V (1983) The impulsive phase of solar flares. II. Characteristics of the hard X-rays. ApJ 269:715–727, doi:10.1086/161081
Lee J, Gary DE (2000) Solar microwave bursts and injection pitch-angle distribution of flare electrons. ApJ 543:457–471
Lee MA, Ryan JM (1986) Time-dependent coronal shock acceleration of energetic solar flare particles. ApJ 303:829–842, doi:10.1086/164131
Lenters GT, Miller JA (1998) Electron acceleration in solar flares by fast-mode waves: coulomb collisions. ApJ 493:451–+, doi:10.1086/305127
Lin RP (1970) The emission and propagation of 40 keV solar flare electrons. II. The electron emission structure of large active regions. Solar Phys 15:453
Lin RP, Schwartz RA, Pelling RM, Hurley KC (1981) A new component of hard X-rays in solar flares. ApJL 251:L109–L114, doi:10.1086/183704
Lin RP, Dennis BR, Hurford GJ, Smith DM, Zehnder A, Harvey PR, Curtis DW, Pankow D, Turin P, Bester M, Csillaghy A, Lewis M, Madden N, van Beek HF, Appleby M, Raudorf T, McTiernan J, Ramaty R, Schmahl E, Schwartz R, Krucker S, Abiad R, Quinn T, Berg P, Hashii M, Sterling R, Jackson R, Pratt R, Campbell RD, Malone D, Landis D, Barrington-Leigh CP, Slassi-Sennou S, Cork C, Clark D, Amato D, Orwig L, Boyle R, Banks IS, Shirey K, Tolbert AK, Zarro D, Snow F, Thomsen K, Henneck R, Mchedlishvili A, Ming P, Fivian M, Jordan J, Wanner R, Crubb J, Preble J, Matranga M, Benz A, Hudson H, Canfield RC, Holman GD, Crannell C, Kosugi T, Emslie AG, Vilmer N, Brown JC, Johns-Krull C, Aschwanden M, Metcalf T, Conway A (2002) The reuven ramaty high-energy solar spectroscopic imager (RHESSI). Solar Phys 210:3–32, doi:10.1023/A:1022428818870
Lin RP, Krucker S, Hurford GJ, Smith DM, Hudson HS, Holman GD, Schwartz RA, Dennis BR, Share GH, Murphy RJ, Emslie AG, Johns-Krull C, Vilmer N (2003) RHESSI observations of particle acceleration and energy release in an intense solar gamma-ray line flare. ApJL 595:L69–L76, doi:10.1086/378932

Litvinenko YE (2006) Three-dimensional fan magnetic reconnection and particle acceleration in the solar corona. A&A 452:1069–1074, doi:10.1051/0004-6361:20054324
Litvinenko YE, Somov BV (1993) Particle acceleration in reconnecting current sheets. Solar Phys 146:127–133
Liu W, Petrosian V, Dennis BR, Jiang YW (2008) Double coronal Hard and Soft X-ray source observed by RHESSI: evidence for magnetic reconnection and particle acceleration in solar flares. ApJ 676:704–716, doi:10.1086/527538, arXiv:0709.1963
MacKinnon AL (1988) Coulomb collisional precipitation of fast electrons in solar flares. A&A 194: 279–287
MacKinnon AL (1991) Collisional scattering of fast electrons in a coronal magnetic bottle. A&A 242:256–270
Mann G, Classen HT, Motschmann U (2001) Generation of highly energetic electrons by shock waves in the solar corona. JGR 106:25,323–25,332, doi:10.1029/2000JA004010
Mann G, Aurass H, Warmuth A (2006) Electron acceleration by the reconnection outflow shock during solar flares. A&A 454:969–974, doi:10.1051/0004-6361:20064990
Martens PCH, Young A (1990) Neutral beams in two-ribbon flares and in the geomagnetic tail. ApJS 73:333–342, doi:10.1086/191469
Masuda S (1994) Hard X-ray sources and the primary energy release site in solar flares. PhD thesis, Dissertation, *Yohkoh*/HXT group, NAO, Mitaka (1994)
Masuda S, Kosugi T, Hara H, Tsuneta S, Ogawara Y (1994) A loop-top hard X-ray source in a compact solar flare as evidence for magnetic reconnection. Nature 371:495, doi:10.1038/371495a0
McClements KG (1990) A Fokker–Planck description of the trapping and precipitation of fast electrons in solar flares. A&A 234:487–495
McComas DJ, Phillips JL, Hundhausen AJ, Burkepile JT (1992) Disconnection of open coronal magnetic structures. In: Marsch E, Schwenn R (eds) Solar wind seven colloquium, pp 225–228
McKenzie DL (1975) Hard X-ray bursts from flare behind the solar limb. Solar Phys 40:183–191
McKenzie DE, Hudson HS (1999) X-ray observations of motions and structure above a solar flare arcade. ApJL 519:L93–L96, doi:10.1086/312110
Melrose DB, Brown JC (1976) Precipitation in trap models for solar hard X-ray bursts. MNRAS 176:15–30
Mewaldt RA, Cohen CMS, Labrador AW, Leske RA, Mason GM, Desai MI, Looper MD, Mazur JE, Selesnick RS, Haggerty DK (2005) Proton, helium, and electron spectra during the large solar particle events of October–November 2003. J Geophys Res (Space Physics) 110:9–+, doi:10.1029/2005JA011038
Miller JA (1997) Electron acceleration in solar flares by fast mode waves: quasi-linear theory and pitch-angle scattering. ApJ 491:939, doi:10.1086/305004
Miller JA, Ramaty R (1987) Ion and relativistic electron acceleration by Alfven and whistler turbulence in solar flares. Solar Phys 113:195–200
Miller JA, Roberts DA (1995) Stochastic proton acceleration by cascading alfven waves in impulsive solar flares. ApJ 452:912, doi:10.1086/176359
Miller JA, Larosa TN, Moore RL (1996) Stochastic electron acceleration by cascading fast mode waves in impulsive solar flares. ApJ 461:445, doi:10.1086/177072
Miller JA, Cargill PJ, Emslie AG, Holman GD, Dennis BR, LaRosa TN, Winglee RM, Benka SG, Tsuneta S (1997) Critical issues for understanding particle acceleration in impulsive solar flares. JGR 102:14631–14660, doi:10.1029/97JA00976
Moses D, Dröge W, Meyer P, Evenson P (1989) Characteristics of energetic solar flare electron spectra. ApJ 346:523–530
Murphy RJ, Dermer CD, Ramaty R (1987) High-energy processes in solar flares. ApJS 63:721–748
Neupert WM (1968) Comparison of solar X-ray line emission with microwave emission during flares. ApJ 153:L59
Nitta N, Dennis BR, Kiplinger AL (1990) X-ray observations of two short but intense solar flares. ApJ 353:313–322, doi:10.1086/168618
Nitta NV, Sato J, Hudson HS (2001) The physical nature of the loop-top X-ray sources in the gradual phase of solar flares. ApJ 552:821–832, doi:10.1086/320547
Onofri M, Isliker H, Vlahos L (2006) Stochastic acceleration in turbulent electric fields generated by 3D reconnection. Phys Rev Lett 96(15):151,102, doi:10.1103/PhysRevLett.96.151102, astro-ph/0604192
Palmer ID, Smerd SF (1972) Evidence for a two-component injection of cosmic rays from the solar flare of 1969, March 30. Solar Phys 26:460
Parker EN (1983) Magnetic neutral sheets in evolving fields. Part Two: Formation of the solar corona. ApJ 264:642, doi:10.1086/160637

Parks GK, Winckler JR (1969) Sixteen-second periodic pulsations observed in the correlated microwave and energetic X-ray emission from a solar flare. ApJ 155:L117

Petrosian V, Donaghy TQ (1999) On the spatial distribution of Hard X-rays from solar flare loops. ApJ 527:945–957, arXiv:astro-ph/9907181

Petrosian V, Liu S (2004) Stochastic acceleration of electrons and protons. I. Acceleration by parallel-propagating waves. ApJ 610:550–571, doi:10.1086/421486, arXiv:astro-ph/0401585

Petrosian V, Donaghy TQ, McTiernan JM (2002) Loop top hard X-ray emission in solar flares: images and statistics. ApJ 569:459–473, doi:10.1086/339240, astro-ph/0112363

Phillips KJH (2004) The solar flare 3.8–10 keV X-ray spectrum. ApJ 605:921–930, doi:10.1086/382523

Pick M, Forbes TG, Mann G, Cane HV, Chen J, Ciaravella A, Cremades H, Howard RA, Hudson HS, Klassen A, Klein KL, Lee MA, Linker JA, Maia D, Mikic Z, Raymond JC, Reiner MJ, Simnett GM, Srivastava N, Tripathi D, Vainio R, Vourlidas A, Zhang J, Zurbuchen TH, Sheeley NR, Marqué C (2006) Multi-wavelength observations of CMEs and associated phenomena. Space Sci Rev 123:341–382, doi:10.1007/s11214-006-9021-1

Pryadko JM, Petrosian V (1997) Stochastic acceleration of low-energy electrons in cold plasmas. ApJ 482:774–+, doi:10.1086/304168, arXiv:astro-ph/9610148

Ramaty R (1979) Energetic particles in solar flares. In: Arons J, McKee C, Max C (eds) Particle acceleration mechanisms in astrophysics, American Institute of Physics Conference Series, vol 56, pp 135–154

Reames DV (1999) Particle acceleration at the Sun and in the heliosphere. Space Sci Rev 90:413–491, doi:10.1023/A:1005105831781

Rieger E, Reppin C, Kanbach G, Forrest DJ, Chupp EL, Share GH (1983) Solar flares with photon emission above 10 MeV—measurements with the gamma ray experiment on board the SMM-satellite. In: International cosmic ray conference, vol 10, pp 338–341

Roy JR, Datlowe DW (1975) X-ray bursts from solar flares behind the limb. Solar Phys 40:165–182

Rybicki GB, Lightman AP (1979) Radiative processes in astrophysics. Wiley, New York

Sakao T (1994) Characteristics of solar flare hard X-ray sources as revealed with the Hard X-ray Telescope aboard the *Yohkoh* satellite. PhD thesis, University of Tokyo

Saldanha R, Krucker S, Lin RP (2008) Hard X-ray spectral evolution and production of solar energetic particle events during the January 2005 X-class flares. ApJ 673:1169–1173, doi:10.1086/524929

Sato J, Matsumoto Y, Yoshimura K, Kubo S, Kotoku J, Masuda S, Sawa M, Suga K, Yoshimori M, Kosugi T, Watanabe T (2006) *Yohkoh*/WBS Recalibration and a comprehensive catalogue of solar flares observed by *Yohkoh* SXT, HXT and WBS instruments. Solar Phys 236:351–368, doi:10.1007/s11207-006-1831-5

Sheeley NR Jr, Warren HP, Wang YM (2004) The origin of postflare loops. ApJ 616:1224–1231, doi:10.1086/425126

Shibata K (1996) New observational facts about solar flares from studies—*Yohkoh* evidence of magnetic reconnection and a unified model of flares. Adv Space Res 17:9

Shibata K, Masuda S, Shimojo M, Hara H, Yokoyama T, Tsuneta S, Kosugi T, Ogawara Y (1995) Hot-plasma ejections associated with compact-loop solar flares. ApJL 451:L83+, doi:10.1086/309688

Simnett GM (2003) Energetic particles and coronal mass ejections: a case study from ace and ulysses. Solar Phys 213:387–412

Smith DM, Lin RP, Turin P, Curtis DW, Primbsch JH, Campbell RD, Abiad R, Schroeder P, Cork CP, Hull EL, Landis DA, Madden NW, Malone D, Pehl RH, Raudorf T, Sangsingkeow P, Boyle R, Banks IS, Shirey K, Schwartz R (2002) The RHESSI spectrometer. Solar Phys 210:33–60, doi:10.1023/A:1022400716414

Somov BV, Bogachev SA (2003) The betatron effect in collapsing magnetic traps. Astron Lett 29:621–628, doi:10.1134/1.1607500

Somov BV, Kosugi T (1997) Collisionless reconnection and high-energy particle acceleration in solar flares. ApJ 485:859

Speiser TW, Lyons LR (1984) Comparison of an analytical approximation for particle motion in a current sheet with precise numerical calculations. JGR 89:147–158

Sprangle P, Vlahos L (1983) Electron cyclotron wave acceleration outside a flaring loop. ApJL 273:L95–L99, doi:10.1086/184137

Stepanov AV, Tsap Y (2002) Electron–whistler interaction in coronal loops and radiation signatures. Solar Phys 211:135–154

Stepanov AV, Yokoyama T, Shibasaki K, Melnikov VF (2007) Turbulent propagation of high-energy electrons in a solar coronal loop. A&A 465:613–619, doi:10.1051/0004-6361:20066573

Strong KT, Benz AO, Dennis BR, Poland AI, Leibacher JW, Mewe R, Schrijver J, Simnett G, Smith JBJr, Sylwester J (1984) A multiwavelength study of a double impulsive flare. Solar Phys 91:325–344
Sturrock PA (1966) Model of the high-energy phase of solar flares. Nature 211:695
Sui L, Holman GD (2003) Evidence for the formation of a large-scale current sheet in a solar flare. ApJL 596:L251–L254, doi:10.1086/379343
Sui L, Holman GD, Dennis BR (2004) Evidence for magnetic reconnection in three homologous solar flares observed by RHESSI. ApJ 612:546–556, doi:10.1086/422515
Sui L, Holman GD, Dennis BR (2006) Motion of 3–6 keV nonthermal sources along the legs of a flare loop. ApJL 645:L157–L160, doi:10.1086/506325
Svestka ZF, Fontenla JM, Machado ME, Martin SF, Neidig DF (1987) Multi-thermal observations of newly formed loops in a dynamic flare. Solar Phys 108:237–250
Švestka Z, Fárník F, Hudson HS, Hick P (1998) Large-scale active coronal phenomena in *Yohkoh*/SXT images IV. Solar wind streams from flaring active regions. Solar Phys 182:179–193, doi:10.1023/A:1005033717284
Takakura T, Inda M, Makishima K, Kosugi T, Sakao T, Masuda S, Sakurai T, Ogawara Y (1993) Time variation of the hard X-ray image during the early phase of solar impulsive bursts. PASJ 45:737–753
Tanaka K (1986) Solar flare X-ray spectra of Fe XXVI and Fe XXV from the HINOTORI satellite. PASJ 38:225–249
Tomczak M (2001) The analysis of hard X-ray radiation of flares with occulted footpoints. A&A 366:294–305, doi:10.1051/0004-6361:20000204
Trakhtengerts VY (1984) Relaxation of a plasma with anisotropic velocity distribution. In: Galeev AA, Sudan RN (eds) Basic plasma physics: selected chapters, Handbook of Plasma Physics, vol 1, p 519
Trottet G, Vilmer N (1984) Electron spectra deduced from solar hard X-ray bursts. Adv Space Res 4:153–156, doi:10.1016/0273-1177(84)90305-3
Tsuneta S, Naito T (1998) Fermi acceleration at the fast shock in a solar flare and the impulsive loop-top Hard X-ray source. ApJL 495:L67+, doi:10.1086/311207, arXiv:astro-ph/9801109
Tsuneta S, Masuda S, Kosugi T, Sato J (1997) Hot and superhot plasmas above an impulsive flare loop. ApJ 478:787, doi:10.1086/303812
Tucker RJ (1975) Radiation processes in astrophysics. MIT Press, Cambridge
Turkmani R, Vlahos L, Galsgaard K, Cargill PJ, Isliker H (2005) Particle acceleration in stressed coronal magnetic fields. ApJL 620:L59–L62, doi:10.1086/428395
Turkmani R, Cargill PJ, Galsgaard K, Vlahos L, Isliker H (2006) Particle acceleration in stochastic current sheets in stressed coronal active regions. A&A 449:749–757, doi:10.1051/0004-6361:20053548
van Ballegooijen AA (1986) Cascade of magnetic energy as a mechanism of coronal heating. ApJ 311:1001–1014, doi:10.1086/164837
van Beek HF, Hoyng P, Lafleur B, Simnett GM (1980) The Hard X-ray imaging spectrometer/HXIS/. Solar Phys 65:39–52
van den Oord GHJ (1990) The electrodynamics of beam/return current systems in the solar corona. A&A 234:496–518
Veronig AM, Brown JC (2004) A coronal thick-target interpretation of two Hard X-ray loop events. ApJL 603:L117–L120, doi:10.1086/383199
Veronig AM, Brown JC, Bone L (2005a) Evidence for a solar coronal thick-target hard X-ray source observed by RHESSI. Adv Space Res 35:1683–1689, doi:10.1016/j.asr.2005.01.065
Veronig AM, Brown JC, Dennis BR, Schwartz RA, Sui L, Tolbert AK (2005b) Physics of the Neupert effect: estimates of the effects of source energy, mass transport, and geometry using RHESSI and GOES data. ApJ 621:482–497, doi:10.1086/427274
Veronig AM, Karlický M, Vršnak B, Temmer M, Magdalenić J, Dennis BR, Otruba W, Pötzi W (2006) X-ray sources and magnetic reconnection in the X3.9 flare of 2003 November 3. A&A 446:675–690, doi:10.1051/0004-6361:20053112
Vilmer N, Kane SR, Trottet G (1982) Impulsive and gradual hard X-ray sources in a solar flare. A&A 108:306–313
Vilmer N, MacKinnon AL, Trottet G, Barat C (2003) High energy particles during the large solar flare of 1990 May 24: X/gamma ray observations. A&A 412:865–874
Wang T, Sui L, Qiu J (2007) Direct observation of high-speed plasma outflows produced by magnetic reconnection in solar impulsive events. ApJL 661:L207–L210, doi:10.1086/519004
Warren HP (2006) Multithread hydrodynamic modeling of a solar flare. ApJ 637:522–530, doi:10.1086/497904, arXiv:astro-ph/0507328

Warren HP, Bookbinder JA, Forbes TG, Golub L, Hudson HS, Reeves K, Warshall A (1999) TRACE and *Yohkoh* observations of high-temperature plasma in a two-ribbon limb flare. ApJL 527:L121–L124, doi:10.1086/312410

Watko JA, Klimchuk JA (2000) Width variations along coronal loops observed by TRACE. Solar Phys 193:77–92

Wheatland MS, Melrose DB (1995) Interpreting *Yohkoh* hard and soft X-ray flare observations. Solar Phys 158:283–299

White SM, Krucker S, Shibasaki K, Yokoyama T, Shimojo M, Kundu MR (2003) Radio and Hard X-ray images of high-energy electrons in an X-class solar flare. ApJL 595:L111–L114, doi:10.1086/379274

Wild JP, Smerd SF, Weiss AA (1963) Solar bursts. ARAA 1:291, doi:10.1146/annurev.aa.01.090163.001451

Wilhelm K, Curdt W, Marsch E, Schühle U, Lemaire P, Gabriel A, Vial JC, Grewing M, Huber MCE, Jordan SD, Poland AI, Thomas RJ, Kühne M, Timothy JG, Hassler DM, Siegmund OHW (1995) SUMER—Solar ultraviolet measurements of emitted radiation. Solar Phys 162:189–231, doi:10.1007/BF00733430

Zirin H, Ingham W, Hudson H, McKenzie D (1969) De-occultation X-ray events of 2 December, 1967. Solar Phys 9:269–277. doi:10.1007/BF02391648

Zharkova VV, Gordovskyy M (2005) Energy spectra of particles accelerated in a reconnecting current sheet with the guiding magnetic field. MNRAS 356:1107–1116. doi:10.1111/j.1365-2966.2004.08532.x, http://adsabs.harvard.edu/abs/2005MNRAS.356.1107Z